

# The Spin of the Black Hole Microquasar XTE J1550–564 via the Continuum-Fitting and Fe-Line Methods

James F. Steiner<sup>1\*</sup>, Rubens C. Reis<sup>2†</sup>, Jeffrey E. McClintock<sup>1</sup>, Ramesh Narayan<sup>1</sup>, Ronald A. Remillard<sup>3</sup>, Jerome A. Orosz<sup>4</sup>, Lijun Gou<sup>1</sup>, Andrew C. Fabian<sup>2</sup>, Manuel A. P. Torres<sup>1,5</sup>

<sup>1</sup>Harvard-Smithsonian Center for Astrophysics, 60 Garden Street, Cambridge, MA 02138.

<sup>2</sup>Institute of Astronomy, Cambridge University, Madingley Road, Cambridge, CB3 0HA

<sup>3</sup>MIT Kavli Institute for Astrophysics and Space Research, MIT, 70 Vassar Street, Cambridge, MA 02139.

<sup>4</sup>Department of Astronomy, San Diego State University, 5500 Campanile Drive, San Diego, CA 92182-1221.

<sup>5</sup>SRON, Netherlands Institute for Space Research, Sorbonnelaan 2, 3584 CA, Utrecht, The Netherlands.

4 November 2018

## ABSTRACT

We measure the spin of XTE J1550–564 in two ways: by modelling the thermal continuum spectrum of the accretion disc, and independently by modeling the broad red wing of the reflection fluorescence Fe- $K\alpha$  line. We find that the spin measurements conducted independently using both leading methods are in agreement with one another. For the continuum-fitting analysis, we use a data sample consisting of several dozen *RXTE* spectra, and for the Fe- $K\alpha$  analysis, we use a pair of *ASCA* spectra from a single epoch. Our spin estimate for the black hole primary using the continuum-fitting method is  $-0.11 < a_* < 0.71$  (90 per cent confidence), with a most likely spin of  $a_* = 0.34$ . In obtaining this result, we have thoroughly explored the dependence of the spin value on a wide range of model-dependent systematic errors and observational errors; our precision is limited by uncertainties in the distance and orbital inclination of the system. For the Fe-line method, our estimate of spin is  $a_* = 0.55^{+0.15}_{-0.22}$ . Combining these results, we conclude that the spin of this black hole is moderate,  $a_* = 0.49^{+0.13}_{-0.20}$ , which suggests that the jet of this microquasar is powered largely by its accretion disc rather than by the spin energy of the black hole.

**Key words:** accretion, accretion discs — black hole physics — stars: individual XTE J1550–564 — X-rays: binaries.

## 1 INTRODUCTION

During its principal 1998–1999 outburst cycle, the bright X-ray transient XTE J1550–564 produced one of the most remarkable flare events ever observed for a black hole binary. For  $\approx 1$  day, the source intensity rose fourfold relative to neighbouring plateau values, reaching 6.8 Crab. The flux in the dominant power-law component rose by the same factor, and then just as quickly its intensity declined (Sobczak et al. 2000; McClintock et al. 2009). Four days later, AU-scale superluminal radio jets were observed (Hannikainen et al. 2009). Their separation angle ( $\sim 255$  mas) and relative velocity ( $\sim 65$  mas d<sup>-1</sup>) links the birth of these jets to the impulsive X-ray flare. The subsequent detection of large-

scale radio jets in 2000 led to the discovery of relativistic X-ray jets (Corbel et al. 2002). All of the available evidence strongly indicates that these pc-scale X-ray and radio jets were produced by the unique 7-Crab flare event, and we adopt this view.

The microquasar XTE J1550–564 (hereafter J1550) is further distinguished by a pair of high-frequency X-ray oscillations with a 2:3 frequency ratio (184 and 276 Hz; Remillard et al. 2002). During its 1998–1999 eruption, J1550 displayed all of the active accretion states: hard, steep power law (SPL), thermal dominant (TD) and intermediate (INT; Remillard & McClintock 2006). The X-ray spectral and timing properties of this source have been comprehensively studied by many authors (e.g., Sobczak et al. 2000; Homan et al. 2001; Remillard et al. 2002; Kubota & Done 2004; Dunn et al. 2010), as have the properties of its

\* E-mail: jsteiner@cfa.harvard.edu

† E-mail: rcr36@ast.cam.ac.uk

radio counterpart (Corbel et al. 2001; Xue et al. 2008; Hannikainen et al. 2009).

Likewise, the optical counterpart of J1550 was the subject of a comprehensive dynamical study by Orosz et al. (2002). The measurement by these authors of a large mass function immediately established J1550 as a dynamically-confirmed black hole binary with a  $\approx 10 M_{\odot}$  black hole primary in a 1.55-day orbit with a late G or early K companion. This dynamical model was recently revisited using new photometric and spectroscopic data (Orosz et al. 2010). Our higher-resolution spectra ( $60 \text{ km s}^{-1}$ ) revealed that the mass ratio is extreme ( $Q \approx 30$ ) and yielded a refined value of the mass function,  $f(M) = 7.65 \pm 0.38 M_{\odot}$ . Of central importance to the present paper, Orosz et al. (2010) report accurate values of the three key quantities that are essential for determining the spin of the black hole via the continuum fitting method, namely the distance  $D = 4.38_{-0.41}^{+0.58}$  kpc, black hole mass  $M = 9.10 \pm 0.61 M_{\odot}$ , and orbital inclination angle  $i = 74^{\circ} 7 \pm 3^{\circ} 8$ .

Currently, the two principal methods for measuring black hole spin<sup>1</sup> are modeling the thermal spectrum of the accretion disc (Zhang et al. 1997) and modeling the profile of the Fe- $K\alpha$  line (Fabian et al. 1989; Laor 1991). For both methods, spin is measured by estimating the inner radius of the accretion disc  $r_{\text{in}} \equiv R_{\text{in}}/M$  in standard GR units ( $G = c = 1$ ).  $R_{\text{in}}$  is identified with the radius of the innermost stable circular orbit ( $R_{\text{ISCO}}$ ) of the gravitational potential and is related to spin via a monotonic mapping between the dimensionless ISCO radius  $R_{\text{ISCO}}/M$  and the dimensionless spin parameter  $a_*$  (Shapiro & Teukolsky 1983). Strong support for linking  $R_{\text{in}}$  to  $R_{\text{ISCO}}$  is provided by decades of empirical evidence that  $r_{\text{in}}$  is constant in disc-dominated states of black hole binaries (e.g., Tanaka & Lewin 1995), as shown most compellingly in our recent study of the persistent source LMC X-3 (Steiner et al. 2010). Theoretical support for identifying  $R_{\text{in}}$  with  $R_{\text{ISCO}}$  is provided by MHD simulations of thin accretion discs (Reynolds & Fabian 2008; Shafee et al. 2008; Penna et al. 2010; but see Noble et al. 2009, 2010). In short, the relationship for thin accretion discs between  $r_{\text{in}}$ ,  $R_{\text{ISCO}}$  and  $a_*$  is the foundation of both the continuum-fitting and Fe- $K\alpha$  methods of measuring spin.

In the continuum-fitting (CF) method, one determines  $R_{\text{ISCO}}$ , and hence  $a_*$ , via measurements of X-ray temperature and luminosity (i.e., using X-ray flux, distance  $D$  and inclination angle  $i$ ) of the disc emission. In order to obtain reliable values of  $a_*$ , it is essential to (1) select X-ray spectra that have a strong thermal component and (2) have accurate estimates of  $D$ ,  $M$  and  $i$ , like those given above for J1550. In practice, we fit the X-ray spectrum of the black hole’s accretion disc to our version of the Novikov-Thorne thin accretion disc model (Novikov & Thorne 1973; Li et al. 2005; McClintock et al. 2006) using an advanced treatment of spectral hardening (Davis et al. 2005; Davis & Hubeny 2006). In this way, we have measured the spins of six other

stellar black holes. We find spins ranging from  $a_* \approx 0.1$  (Gou et al. 2010) to  $a_* > 0.98$  (McClintock et al. 2006); four other spin values are relatively high,  $a_* \approx 0.7 - 0.9$  (Shafee et al. 2006; Liu et al. 2008, 2010; Gou et al. 2009).

In the Fe- $K\alpha$  method, one determines  $R_{\text{ISCO}}$  by modeling the profile of reflection-fluorescent features in the disc. Most prominent is the broad and skewed iron line, whose shape is determined by Doppler effects, light bending, and gravitational redshift (Reynolds & Nowak 2003). Of central importance is the effect of the redshift on the red wing of the line. This wing extends to very low energies for a rapidly rotating black hole ( $a_* \sim 1$ ) because in this case gas can orbit near the event horizon, deep in the potential well of the black hole. Relative to the CF method, measuring the extent of this red wing in order to infer  $a_*$  is hindered by the relative faintness of the signal. However, the Fe- $K\alpha$  method has the virtues that it is independent of  $M$  and  $D$ , while the blue wing of the line even allows an estimate of  $i$ . What makes the Fe- $K\alpha$  method enormously important is that it is the primary approach to measuring the spins of supermassive black holes in AGN. The spins of several stellar black holes (Reis et al. 2009, 2010; Miller et al. 2009; Blum et al. 2009) and supermassive black holes (Brenneman & Reynolds 2006; Schmoll et al. 2009; Miniutti et al. 2009; Fabian et al. 2009; Zoghbi et al. 2010) have been reported using the Fe line method with values ranging from  $a_* \approx 0$  to  $a_* > 0.98$ .

Knowledge of black hole spin has broad importance to astrophysics: For example, spin is central to most of the many theories of relativistic jets observed for both microquasars and AGN (Blandford & Znajek 1977), and it is comparably important to collapsar models of long GRBs (Woosley 1993) and models of black hole formation and black hole binary evolution (Lee et al. 2002). Hierarchical models for the growth of supermassive black holes require knowledge of the spin distributions of the merging partners (Volonteri et al. 2005; Berti & Volonteri 2008), and the observed properties of AGN may be strongly conditioned by black hole spin (McNamara et al. 2009; Garofalo et al. 2010; Tchekhovskoy et al. 2010). Spin measurements are likewise important to gravitational-wave astronomy in predicting the waveforms of merging black holes (Campanelli et al. 2006). Knowledge of black hole spin is becoming important to fundamental physics as well, and enlivening questions are being asked: e.g., Is the No-Hair Theorem valid and can it be tested (Johannsen & Psaltis 2010)? Do we live in a string axiverse filled with light axions (Arvanitaki et al. 2010)?

There have been two prior estimates of the spin of J1550. The first of these,  $a_* \approx 0-0.1$ , was obtained using the CF method and a sample of ten *RXTE* spectra (Davis et al. 2006). This result was based on the old dynamical model with approximate values of  $M$ ,  $i$ , and  $D$  (e.g.,  $D$  was uncertain by  $\approx 45$  per cent; Orosz et al. 2002). We improve upon the work of Davis et al. by using our new dynamical model (e.g., with its fourfold better determination of  $D$ ) and a  $\approx 6$ -times larger sample of *RXTE* spectra, and by our detailed treatment of observational and model-dependent uncertainties. A second ‘preliminary’ spin estimate,  $a_* \approx 0.76$ , was obtained using a spectral model that self-consistently merged the disc-continuum and Fe- $K\alpha$  components, in which the spin result for J1550 was predominately determined by the Fe- $K\alpha$  model (Miller et al. 2009). We will treat the data

<sup>1</sup> Black hole spin is commonly expressed in terms of the dimensionless quantity  $a_* \equiv a/M = cJ/GM^2$ , where  $M$  and  $J$  are respectively the black hole mass and angular momentum (Shapiro & Teukolsky 1983). Its limiting value is  $a_* = +1$  ( $-1$ ) for a maximal Kerr hole rotating in a prograde (retrograde) sense relative to the accretion disc;  $a_* = 0$  corresponds to a non-spinning Schwarzschild hole.

considered in their study, and additional data; however, unlike this exploratory and preliminary study of eight black-hole systems (including J1550), we fixedly focus on J1550 and so are able to refine and improve upon their work.

In this Paper, we present the spin of J1550 on two fronts. After introducing the data sets (§ 2), we begin by first applying the CF technique (§§ 3,4). This work is complemented with a thorough exploration of the statistical and systematic uncertainties inherent to the CF method (§ 5). Next, we measure the spin of J1550 using the Fe- $K\alpha$  technique (§ 6), and we finish with a discussion of the results (§ 7) and our conclusions (§ 8).

## 2 OBSERVATIONS

The primary data set used in this study is a compendium of 347 *Rossi X-ray Timing Explorer* (*RXTE*) observations. The data include those obtained during the bright discovery outburst in 1998–1999 on through four additional minor outbursts, the last ending in mid-2003. A light curve of the flux, showing the spectral evolution of the source, is presented in Figure 1, where the spectral state assignments have been determined using precisely the model, procedures and criteria described in Remillard & McClintock (2006). Thermal dominant data, which are of primary importance for CF spin measurements, were obtained exclusively during the first outburst cycle.

*RXTE* spectral data are collected using exclusively PCU-2, the best calibrated of the five Proportional Counter Array (PCA) detectors. Spectra are individually obtained by grouping sequential observations into approximately half-day bins with a typical exposure time  $\sim 3$  ks. We follow the procedures described in McClintock et al. (2006): The data are background subtracted, a customary 1 per cent systematic error in the data count rates is included, and a dead time correction ranging from approximately 1 to 20 per cent is applied. Spectra are fitted over the energy range 2.55–45 keV using XSPEC version 12.4–12.6 (the software used throughout this Paper; Arnaud 1996). Calibration over this range is achieved using the latest version of PCARMF (v11.7)<sup>2</sup>.

A linear collimator correction (assuming an ideal  $1^\circ$  triangular response; Jahoda et al. 2006) has been applied to the data set to account for a series of offsets in the PCA pointing. Specifically, we normalised the flux upward by 4.4 per cent (a 2.'67 offset) during the 1998–1999 outburst, and 7.1 per cent (4.'28 offset) during the 2000 outburst. After April 2001 the correction is just  $\sim 0.1$  per cent. In addition to these global corrections, a handful of observations taken between 1998 September 7–9 and on 1999 January 6 were off-target for unknown reasons by  $\approx 0.2^\circ$  and required us to make large corrections (for details, see Steiner et al. 2009). We estimate that the uncertainty in these flux corrections is no more than 1–2 per cent, which has a negligible impact on our spectral fitting results.

In addition to the *RXTE* data set, we also include a 25 ks *ASCA* Gas Imaging Spectrometer (GIS) observation taken on UT 1998 September 23 when the source was in an intermediate state (see the observation time in Fig. 1

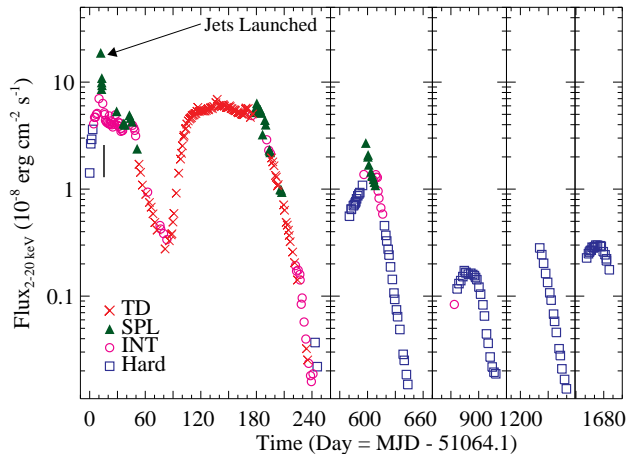


**Figure 1.** A spectral-state encoded 2–20 keV light curve showing all five outburst cycles of J1550. Most disc-dominated data were obtained during the primary outburst in 1998–1999. The time of the *ASCA* observation, which is analysed in § 6, is marked at day 15 by a solid black line. The powerful 7-Crab flare near day 12 was responsible for ejection of superluminal radio jets.

marked by the black vertical line). Following Miller et al. (2009) and Miller et al. (2005), we use these *ASCA* data, with twice the resolution of the *RXTE* PCA data, to examine the iron line. However, we do not report a CF analysis on these data because the Compton component is too strong. We use standard data products for the GIS-2 and GIS-3 spectra with version 4.0 response matrices. The two spectra are fitted jointly over the 1–10 keV energy range, and in § 6 we present our analysis of these data using the Fe- $K\alpha$  method.

## 3 CONTINUUM-FITTING ANALYSIS

We first enumerate our CF data selection requirements and define two tiers of data quality. Next, we introduce the first and principal of three Comptonised accretion-disc models which are applied to the *RXTE* data set. Then, in the following section we introduce two alternative models that differ principally in their treatment of the Compton reflection component. We find very close agreement in the spin estimate using all three models.

### 3.1 *RXTE* Data Selection

We first identify two tiers of quality in our data: first-class ‘gold’ spectra are selected from just the strongly disc-dominated TD-state observations (the most conducive to CF modeling; e.g., Shafee et al. 2006). We additionally consider a broader set of second-tier ‘silver’ spectra which are chosen from either SPL or intermediate states. In order for a spectrum to be assigned to either category, it must pass the Comptonisation strength, quality, and luminosity filters described below.

In our previous work on J1550 and the black-hole candidate H1743–322 (Steiner et al. 2009), we showed that one

<sup>2</sup> <http://www.universe.nasa.gov/xrays/programs/rxte/pca/doc/rmf/pcarmf117.pdf>

to obtain values of  $r_{\text{in}}$  (or equivalently  $a_*$ ) that are consistent with those obtained in the (*gold*) TD state. Based upon this work, we select soft thermal spectra with a power-law normalisation  $f_{\text{SC}} < 25$  per cent, which at  $f_{\text{SC}} \approx 25$  per cent corresponds to a power-law component roughly an order of magnitude stronger than that observed in the TD state. Data fulfilling this broader definition (which are not already in the TD *gold* class) are candidates for the *silver* class.

To be admitted into either category, we require that data meet two additional criteria pertaining to the fit quality and disc luminosity. For quality screening, we adopt a critical goodness-of-fit, defined as  $\chi^2/\nu < 2$ , and also require that the inner-disc radius measurement have a precision better than  $r_{\text{in}}/\sigma_{r_{\text{in}}} = 5$ . We further require that the luminosity of the soft thermal component lie in the range 5–30 per cent  $L_{\text{Edd}}$ . The upper luminosity threshold is required by our thin-disc model (McClintock et al. 2006; Penna et al. 2010). The lower threshold eliminates a regime in which the accretion flow properties may be changing, due to the presence of either advective flows (Esin et al. 1997) or other modes of coronal feedback (e.g., Beloborodov 1999).

### 3.2 Results I: Continuum Fitting using SMEDGE

In selecting our data and for determining the spin, we employ a variant of the principal model that we used in our earlier study of J1550 and H1743–322 (hereafter, Model S; Steiner et al. 2009): CRABCOR×TBABS×SMEDGE(SIMPL⊗KERRBB2).

Here we use TBABS (Wilms et al. 2000) in place of PHABS to describe the low-energy absorption component. We fix the column density to the precise value determined using *Chandra* grating data,  $N_{\text{H}} = 8.0^{+0.4}_{-0.3} \times 10^{21} \text{ cm}^{-2}$  (90 per cent confidence; Miller et al. 2003). The custom multiplicative component CRABCOR simply corrects the response of the PCA detector using our standard reference spectrum of the Crab (see Steiner et al. 2010; Toor & Seward 1974).

The key component of this model is KERRBB2 (McClintock et al. 2006), a fully relativistic thin accretion-disc model, which includes self-irradiation of the disc (‘returning radiation’) and limb darkening (Li et al. 2005). The effects of spectral hardening are incorporated via a pair of look-up tables for the hardening factor  $f$  (Davis et al. 2005; Davis & Hubeny 2006) corresponding to two representative values of the viscosity parameter:  $\alpha = 0.01$  and  $\alpha = 0.1$ . Here and throughout, motivated by the results of both observational data and global GRMHD simulations (Penna et al. 2010; King et al. 2007, and references therein), we adopt  $\alpha = 0.1$  as our fiducial value. Following our previous work, we adopt a zero-torque inner boundary condition and assume alignment of the black hole spin axis with the binary orbital plane; we turn on both limb-darkening and returning radiation flags and fix the normalisation to one. We fix the input parameters  $M$ ,  $i$  and  $D$  to their best-fitting values (§ 1). The model KERRBB2 has just two fit parameters, namely the black hole spin parameter  $a_*$  and the mass accretion rate  $\dot{M}$ , or equivalently,  $r_{\text{in}}$  and the Eddington-scaled bolometric disc luminosity  $L_{\text{D}}/L_{\text{Edd}}$  (McClintock et al. 2006).

We model the power-law component by convolving the thermal component with SIMPL (Steiner et al. 2009), a model that mimics the physics of Compton scattering of

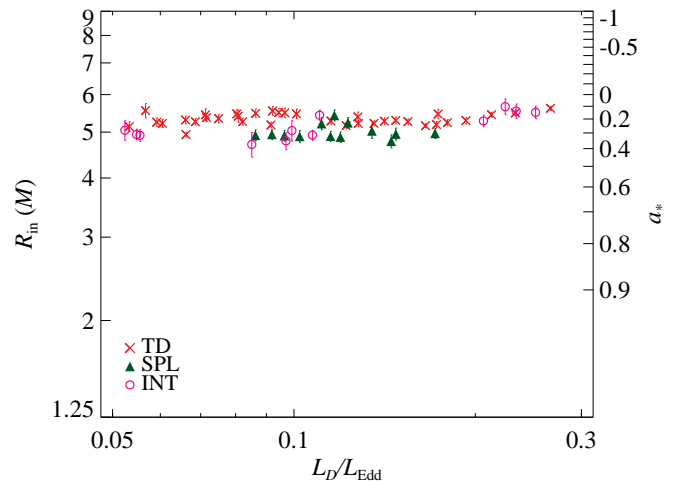


**Figure 2.** The spin, expressed both in terms of  $R_{\text{in}}$  and  $a_*$ , versus luminosity. The TD data comprise the *gold* data set and the intermediate and SPL data the *silver* data set. The mean value of  $R_{\text{in}}$  is in agreement for the two data sets to within  $\approx 5$  per cent even though the Compton component is much stronger for the *silver* data.

thermal disc photons by a hot corona. The model SIMPL converts a fraction  $f_{\text{SC}}$  of the seed photons into a power law with photon index  $\Gamma$ . We use the standard, upscattering-only version. For the reflected component, we assume here that the disc elastically backscatters all incident Compton photons (generated by SIMPL), apart from a broad iron absorption edge feature that is modelled phenomenologically using SMEDGE (Ebisawa et al. 1994). The parameters of SMEDGE are the edge energy  $E_{\text{Edge}}$  (fitted from 7–9 keV), its optical depth  $\tau_{\text{max}}$  (unconstrained in the fit), and the width of the feature  $W_{\text{Edge}}$  (fixed at 7 keV). In the section that follows, we consider two models of reflection that are more physically motivated.

Applying our selection criteria to the full spectral model yields 35 *gold* spectra, where most of the winnowing is a result of our thin-disc limit on the intrinsic luminosity (i.e., prior to scattering) of the accretion-disc component:  $L_{\text{D}}/L_{\text{Edd}} < 0.3$ . We additionally select 25 *silver* spectra, 13 of which correspond to SPL-state observations and 12 to intermediate-state observations. Our spectral-fitting results are summarized in Table 1 (*gold* spectra correspond to entries 1–35 and *silver* to entries 36–60).

For all these selected data, in Figure 2 we plot  $a_*$  versus the luminosity of the disc component  $L_{\text{D}}/L_{\text{Edd}}$ . In a departure from our earlier work, in addition to  $a_*$ , we also plot the inner disc radius  $R_{\text{in}}$ . The two quantities are equivalent in the sense that they are simply related to each other via a monotonic analytical formula (§ 1). We have chosen to also show  $R_{\text{in}}$  because it is the quantity that is more directly determined via continuum fitting.

Figure 2 shows that the *gold* and *silver* data sets give result that are in good agreement. The net weighted result for the combined data set is  $a_* = 0.23 \pm 0.07$  ( $r_{\text{in}} = 5.22 \pm 0.24$ ). The *gold* data give a slightly lower value for the spin,  $a_* = 0.20$ , than do the *silver* data,  $a_* = 0.27$ ; the corresponding shifts in the mean value of  $r_{\text{in}}$  are respectively +2 per cent and –3 per cent.

Although the data are clustered within a few per cent

Table 1. Model S Continuum-Fitting Results

N	MJD	$\frac{L_D}{L_{\text{Edd}}}$	SMEDGE		SIMPL		KERRBB2		$\chi^2_{\nu}/\text{DOF}$	State
			$E_{\text{Edge}}$ (keV)	$\tau_{\text{max}}$	$\Gamma$	$f_{sc}$	$a_*$	$\dot{M}$ ( $10^{18}$ g/s)		
1	51117.4	0.17	8.32 ± 0.14	1.11 ± 0.16	2.06 ± 0.03	0.029 ± 0.002	0.241 ± 0.023	3.30 ± 0.11	0.7/74	TD
2	51119.0	0.15	8.12 ± 0.11	1.34 ± 0.16	2.11 ± 0.03	0.030 ± 0.002	0.220 ± 0.021	3.01 ± 0.09	0.8/74	TD
3	51121.0	0.14	8.26 ± 0.15	1.45 ± 0.25	2.15 ± 0.06	0.011 ± 0.001	0.232 ± 0.019	2.62 ± 0.07	0.7/74	TD
4	51124.7	0.12	8.08 ± 0.13	1.72 ± 0.18	2.15 ± 0.04	0.023 ± 0.001	0.215 ± 0.023	2.25 ± 0.08	0.6/74	TD
5	51128.6	0.10	7.86 ± 0.10	1.71 ± 0.12	2.17 ± 0.03	0.036 ± 0.001	0.161 ± 0.039	2.04 ± 0.10	1.0/74	TD
6	51130.5	0.09	7.98 ± 0.09	1.71 ± 0.09	2.17 ± 0.02	0.038 ± 0.001	0.151 ± 0.034	1.92 ± 0.09	1.3/74	TD
7	51132.5	0.09	7.84 ± 0.10	1.72 ± 0.11	2.16 ± 0.02	0.035 ± 0.001	0.157 ± 0.034	1.75 ± 0.09	0.8/74	TD
8	51134.5	0.08	7.74 ± 0.10	1.85 ± 0.12	2.28 ± 0.03	0.027 ± 0.001	0.161 ± 0.035	1.63 ± 0.08	0.8/74	TD
9	51136.9	0.07	7.84 ± 0.09	2.02 ± 0.11	2.16 ± 0.03	0.025 ± 0.001	0.189 ± 0.031	1.42 ± 0.07	0.9/74	TD
10	51145.5	0.05	7.92 ± 0.10	1.80 ± 0.11	2.05 ± 0.02	0.025 ± 0.001	0.255 ± 0.035	1.01 ± 0.06	0.7/74	TD
11	51150.1	0.06	7.60 ± 0.12	1.80 ± 0.14	2.08 ± 0.03	0.030 ± 0.001	0.223 ± 0.031	1.15 ± 0.06	0.9/74	TD
12	51152.1	0.07	7.94 ± 0.14	2.61 ± 0.26	2.13 ± 0.07	0.015 ± 0.001	0.220 ± 0.024	1.33 ± 0.05	0.8/74	TD
13	51152.9	0.07	8.19 ± 0.11	3.35 ± 0.28	2.20 ± 0.08	0.010 ± 0.001	0.311 ± 0.017	1.21 ± 0.04	0.8/74	TD
14	51154.0	0.08	7.84 ± 0.20	2.78 ± 0.45	2.39 ± 0.13	0.012 ± 0.002	0.220 ± 0.026	1.60 ± 0.06	0.7/74	TD
15	51155.1	0.09	8.44 ± 0.22	2.07 ± 0.39	2.43 ± 0.13	0.008 ± 0.001	0.244 ± 0.021	1.75 ± 0.06	0.7/74	TD
16	51157.6	0.12	8.59 ± 0.41	1.32 ± 0.57	2.75 ± 0.25	0.007 ± 0.002	0.249 ± 0.022	2.33 ± 0.07	0.8/74	TD
17	51160.3	0.17	7.00 ± 2.96	0.14 ± 0.22	1.94 ± 0.27	0.002 ± 0.001	0.249 ± 0.015	3.15 ± 0.07	0.7/74	TD
18	51162.2	0.21	7.59 ± 0.14	1.38 ± 0.26	3.11 ± 0.65	0.004 ± 0.004	0.167 ± 0.020	4.29 ± 0.10	1.1/74	TD
19	51163.2	0.23	7.21 ± 0.16	1.58 ± 0.33	3.20 ± 1.34	0.004 ± 0.008	0.153 ± 0.023	4.74 ± 0.13	0.7/74	TD
20	51164.2	0.27	7.00 ± 0.32	1.34 ± 0.21	2.33 ± 1.12	0.001 ± 0.003	0.117 ± 0.016	5.55 ± 0.11	1.0/74	TD
21	51260.6	0.19	8.12 ± 0.12	1.12 ± 0.20	2.06 ± 0.04	0.030 ± 0.002	0.213 ± 0.025	3.77 ± 0.12	0.4/66	TD
22	51261.8	0.18	8.39 ± 0.16	1.00 ± 0.18	2.03 ± 0.03	0.029 ± 0.002	0.227 ± 0.023	3.48 ± 0.11	0.7/66	TD
23	51263.1	0.17	8.12 ± 0.12	1.42 ± 0.16	2.13 ± 0.03	0.036 ± 0.002	0.162 ± 0.038	3.51 ± 0.16	0.6/66	TD
24	51264.8	0.15	8.21 ± 0.10	1.55 ± 0.15	2.07 ± 0.03	0.031 ± 0.001	0.210 ± 0.025	2.89 ± 0.10	0.7/66	TD
25	51265.6	0.14	8.28 ± 0.12	1.40 ± 0.14	2.09 ± 0.03	0.035 ± 0.002	0.217 ± 0.025	2.75 ± 0.10	0.8/66	TD
26	51266.9	0.13	8.18 ± 0.12	1.60 ± 0.17	2.12 ± 0.03	0.024 ± 0.001	0.233 ± 0.024	2.46 ± 0.09	0.5/66	TD
27	51267.6	0.13	8.14 ± 0.09	1.80 ± 0.11	2.13 ± 0.02	0.040 ± 0.001	0.184 ± 0.038	2.54 ± 0.12	0.9/66	TD
28	51273.6	0.10	8.10 ± 0.08	1.82 ± 0.09	2.17 ± 0.02	0.040 ± 0.001	0.153 ± 0.038	1.96 ± 0.10	0.7/66	TD
29	51274.5	0.09	7.88 ± 0.10	1.91 ± 0.12	2.12 ± 0.03	0.033 ± 0.001	0.138 ± 0.036	1.89 ± 0.10	0.7/66	TD
30	51276.3	0.08	7.96 ± 0.12	2.64 ± 0.22	2.04 ± 0.05	0.019 ± 0.001	0.179 ± 0.047	1.61 ± 0.10	0.6/66	TD
31	51277.4	0.07	7.98 ± 0.10	2.20 ± 0.14	2.07 ± 0.03	0.026 ± 0.001	0.197 ± 0.033	1.48 ± 0.08	1.0/66	TD
32	51278.7	0.07	7.82 ± 0.13	2.03 ± 0.16	2.11 ± 0.04	0.027 ± 0.001	0.168 ± 0.047	1.44 ± 0.10	0.7/66	TD
33	51279.6	0.07	7.93 ± 0.10	2.16 ± 0.13	2.06 ± 0.03	0.023 ± 0.001	0.207 ± 0.029	1.30 ± 0.06	0.8/66	TD
34	51280.6	0.06	8.11 ± 0.12	2.19 ± 0.17	2.06 ± 0.04	0.021 ± 0.001	0.233 ± 0.030	1.17 ± 0.06	0.7/66	TD
35	51283.2	0.06	7.45 ± 0.20	1.57 ± 0.22	2.21 ± 0.05	0.027 ± 0.002	0.135 ± 0.057	1.17 ± 0.10	0.6/66	TD
36	51110.3	0.25	8.32 ± 0.08	1.11 ± 0.09	2.55 ± 0.02	0.223 ± 0.007	0.149 ± 0.049	5.13 ± 0.25	0.8/74	INT
37	51111.6	0.23	8.14 ± 0.10	1.14 ± 0.10	2.50 ± 0.02	0.240 ± 0.009	0.139 ± 0.058	4.79 ± 0.27	0.8/74	INT
38	51112.8	0.22	8.14 ± 0.09	1.16 ± 0.09	2.51 ± 0.02	0.249 ± 0.008	0.103 ± 0.065	4.70 ± 0.29	0.8/74	INT
39	51113.7	0.21	8.32 ± 0.09	1.24 ± 0.10	2.49 ± 0.02	0.208 ± 0.008	0.214 ± 0.044	4.03 ± 0.20	1.0/74	INT
40	51115.3	0.17	8.36 ± 0.08	1.33 ± 0.09	2.42 ± 0.02	0.153 ± 0.005	0.303 ± 0.035	3.14 ± 0.14	0.8/74	SPL
41	51126.6	0.11	8.19 ± 0.08	1.67 ± 0.08	2.29 ± 0.02	0.059 ± 0.001	0.172 ± 0.041	2.21 ± 0.11	1.0/74	INT
42	51140.0	0.06	8.01 ± 0.09	1.75 ± 0.10	2.17 ± 0.02	0.086 ± 0.002	0.316 ± 0.039	1.01 ± 0.07	1.0/74	INT
43	51140.7	0.05	8.13 ± 0.08	1.77 ± 0.09	2.19 ± 0.02	0.078 ± 0.002	0.310 ± 0.036	1.00 ± 0.07	1.1/74	INT
44	51143.8	0.05	8.04 ± 0.09	1.69 ± 0.10	2.21 ± 0.02	0.081 ± 0.003	0.281 ± 0.068	0.98 ± 0.10	0.8/74	INT
45	51269.7	0.12	8.25 ± 0.08	1.83 ± 0.09	2.25 ± 0.02	0.052 ± 0.001	0.173 ± 0.043	2.34 ± 0.13	1.0/66	SPL
46	51270.8	0.09	8.30 ± 0.08	1.64 ± 0.08	2.28 ± 0.01	0.110 ± 0.002	0.309 ± 0.035	1.68 ± 0.09	1.0/66	SPL
47	51271.4	0.09	8.34 ± 0.09	1.48 ± 0.08	2.30 ± 0.02	0.120 ± 0.003	0.315 ± 0.036	1.57 ± 0.09	0.9/66	SPL
48	51664.4	0.15	8.19 ± 0.08	1.50 ± 0.10	2.45 ± 0.02	0.165 ± 0.005	0.307 ± 0.041	2.70 ± 0.15	0.8/66	SPL
49	51664.7	0.15	8.39 ± 0.08	1.42 ± 0.09	2.42 ± 0.02	0.173 ± 0.005	0.354 ± 0.042	2.56 ± 0.15	0.9/66	SPL
50	51665.4	0.13	8.11 ± 0.09	1.46 ± 0.09	2.42 ± 0.02	0.145 ± 0.004	0.286 ± 0.051	2.50 ± 0.16	0.8/66	SPL
51	51667.7	0.12	8.19 ± 0.09	1.48 ± 0.09	2.36 ± 0.02	0.126 ± 0.003	0.327 ± 0.034	2.15 ± 0.11	0.7/66	SPL
52	51668.8	0.12	8.22 ± 0.09	1.46 ± 0.09	2.34 ± 0.02	0.117 ± 0.003	0.322 ± 0.033	2.08 ± 0.10	1.0/66	SPL
53	51669.2	0.12	8.06 ± 0.08	1.61 ± 0.10	2.38 ± 0.02	0.109 ± 0.003	0.228 ± 0.039	2.38 ± 0.13	1.1/66	SPL
54	51670.6	0.10	8.09 ± 0.08	1.58 ± 0.09	2.35 ± 0.02	0.143 ± 0.003	0.323 ± 0.039	1.85 ± 0.11	0.8/66	SPL
55	51670.8	0.11	8.29 ± 0.08	1.56 ± 0.09	2.33 ± 0.02	0.113 ± 0.003	0.314 ± 0.034	1.95 ± 0.10	0.8/66	INT
56	51671.4	0.11	8.03 ± 0.09	1.70 ± 0.10	2.35 ± 0.02	0.108 ± 0.003	0.234 ± 0.044	2.14 ± 0.13	1.1/66	SPL
57	51672.4	0.10	8.22 ± 0.09	1.66 ± 0.09	2.31 ± 0.02	0.121 ± 0.003	0.318 ± 0.036	1.75 ± 0.10	0.8/66	SPL
58	51673.0	0.10	8.24 ± 0.08	1.52 ± 0.07	2.39 ± 0.01	0.205 ± 0.005	0.351 ± 0.055	1.71 ± 0.14	0.7/66	INT
59	51673.4	0.10	8.14 ± 0.08	1.58 ± 0.08	2.42 ± 0.01	0.196 ± 0.004	0.283 ± 0.070	1.84 ± 0.17	0.8/66	INT
60	51674.7	0.09	8.07 ± 0.10	1.39 ± 0.08	2.31 ± 0.02	0.224 ± 0.006	0.374 ± 0.076	1.48 ± 0.16	0.6/66	INT

Note. —

1. Reported error estimates are symmetric  $1\sigma$  statistical uncertainties.
2.  $M$ ,  $i$ , and  $D$  are frozen at their fiducial values.

of a central value of  $r_{\text{in}}$ , there is a small  $\sim 5$  per cent increase with increasing  $L_D$ , which is most pronounced for  $L_D/L_{\text{Edd}} > 0.2$ , a pattern that has been previously observed for other sources (e.g., GRS 1915+105, McClintock et al. 2006; LMC X–3, Steiner et al. 2010). We tentatively attribute this effect to a thickening of the disc with luminosity and the limitation of our razor-thin disc model.

#### 4 CONTINUUM FITTING: TOWARDS A SELF-CONSISTENT DISC + REFLECTION MODEL

In the previous section, we used the empirical model `SMEDGE` to crudely account for a prominent spectral feature in the reflection component, namely, the broad  $K$ -edge of iron. We now consider a more physically-motivated treatment of the full reflection spectrum, which is generated by that portion of the power-law flux that strikes the accretion disc (Ross & Fabian 1993). We first consider a generalised version of `SIMPL` that is more appropriate to the problem at hand. We then examine two reflection models, `IREFLECT`, and `REFLIONX`, concluding that the former model is better for CF fitting, while the latter model is better for fitting the profile of the  $\text{Fe-}K\alpha$  line (which is considered in § 6). As we describe below, there is presently no unified reflection model that is well-suited to both approaches of measuring spin.

##### 4.1 A Variant of the Power-Law Model `SIMPL`

As in § 3, the core of our model consists of `KERRBB2` and `SIMPL`. However, we now introduce a modified version of `SIMPL` that is appropriate when including a separate and additive reflection component. This model, `SIMPL-R`, is a generalisation of `SIMPL` that covers the two limiting cases described by equations 1 & 2 in Steiner et al. (2009), and applies to intermediate cases as well:

$$n_{\text{out}}(E)dE = (1 - f_{\text{SC}})n_{\text{in}}(E)dE + (f_{\text{SC}}/x) \left[ \int_{E_{\text{min}}}^{E_{\text{max}}} n_{\text{in}}(E_0)G(E; E_0)dE_0 \right] dE. \quad (1)$$

Here,  $n_{\text{in}}(E)$  and  $n_{\text{out}}(E)$  are the seed input and model output photon number densities at energy ( $E$ ). Again, the normalisation constant  $f_{\text{SC}}$  is the fraction of photons directed into a power law with photon index  $\Gamma$ , and  $G(E; E_0)$  is the distribution function of the output power law (see Steiner et al. 2009; Ebisawa 1999). The one new parameter is  $x$ , which determines the fraction of the power-law photons that strike the disc. *These are the photons which will be considered in modeling the reflection component.*

The standard version of `SIMPL`, which was used in the preceding section, assumes that none of the Compton-scattered photons strike the disc, or adopting an equivalent interpretation, that reflection acts like a perfect mirror with no absorption. This corresponds to the limiting case  $x = 1$ , which is described by Equation 1 in Steiner et al. (2009). In the opposite limit,  $x = 2$ , half of the scattered photons are redirected downward, illuminating the disc, while failing to reach an observer at infinity. As they encounter the disc atmosphere, the returning photons are absorbed and reprocessed, thereby generating the reflection component. This limit corresponds to Equation 2 in Steiner et al. (2009).

The variant `SIMPL-R` (Eq. 1) generalises this dichotomy, making it possible to treat separately the reprocessed emission coming from the illuminated disc via the tunable parameter  $x$ . This allows one to model a corona quite generally. The quantity  $x - 1$  describes the solid angle subtended by the disc from the perspective of the corona in units of  $2\pi$ , which we refer to as a covering factor. In this paper, we assume that the geometry of the corona is a disc-hugging slab with

a covering factor of unity ( $x = 2$ ); thus, half the photons escape the system and half strike the disc. As shorthand, we will refer to the portion of the Compton component produced by `SIMPL-R` which irradiates the disc as `SIMPLC` (e.g., the second term on the right-hand side of Eq. 1 multiplied by the covering factor).

##### 4.2 Results II: Continuum Fitting using `IREFLECT` and `REFLIONX`

We first consider the model `IREFLECT` (Magdziarz & Zdziarski 1995), which computes the reflected spectrum (including scattering and edge absorption, but excluding line fluorescence) generated in an ionised disc atmosphere that is illuminated by an arbitrary external spectrum. We convolve the disc-illuminating component `SIMPLC` with `IREFLECT` and isolate the reflected component by setting the parameter `rel_refl` to -1. (Our model implicitly assumes that the observed and illuminating power-law spectra are identical.) The ionisation parameter  $\xi \equiv L/nR^2$  is initially set to  $10^4$  and allowed to vary freely from  $10^1 - 10^5$ , while the characteristic disc temperature is fixed to  $T_{\text{disc}} = 5 \times 10^6$  K and the metallicity is assumed to be solar.  $\text{Fe-}K\alpha$  emission is included separately in an approximate fashion as an intrinsically narrow Gaussian line centred at a restframe energy of 6.5 keV. This composite reflection component is then convolved with the relativistic smearing kernel `KERRCONV` (Brenneman & Reynolds 2006) with the radial emissivity index  $q$  fixed at the best-fitting `RXTE` value  $q = 2.5$  (see § 6). The complete model, which is comprised of an accretion-disc and a power-law component, is: `CRABCOR×TBABS(SIMPL-R⊗KERRBB2 + KERRCONV⊗(IREFLECT⊗SIMPLC + GAUSS))`.

The primary limitation of this model (referred to hereafter as Model I) is that although edges are included, the fluorescent line features (e.g., García & Kallman 2010), apart from  $\text{Fe-}K\alpha$ , are missing. Also, the strength of the  $\text{Fe-}K\alpha$  feature should be tied to the depth of the corresponding edge feature, but here that is not possible. Below and in § 5, we will demonstrate that these shortcomings of Model I have little effect on the CF spin results because for our primary *gold* spectra the reflected component is faint compared to the dominant thermal component. However, these issues are of critical importance in estimating spin via the  $\text{Fe-}K\alpha$  line (§ 6).

We now consider a second reflection model, `REFLIONX` (Ross & Fabian 2005), which we use as a replacement for `(IREFLECT⊗SIMPLC+GAUSS)` in Model I given above. We will refer to the new composite model as Model R. In `REFLIONX`, reflection is produced by a power-law spectrum illuminating a cold slab of constant density. The virtue of this model is that it properly couples line emission to absorption, and it also describes the full  $\text{Fe-}K$  emission-line complex. A major drawback is that it is optimized for modeling AGN, which have cold discs of lower density. Consequently, in estimating spin via the  $\text{Fe-}K\alpha$  method (§ 6), we use a high-density variant of `REFLIONX`, `REFBHB`, which includes an intrinsic blackbody component (Ross & Fabian 2007). Because the blackbody component is hardwired into `REFBHB`, it can not presently be used with CF models. We therefore use `REFLIONX` in concert with `KERRBB2` for our CF analysis.

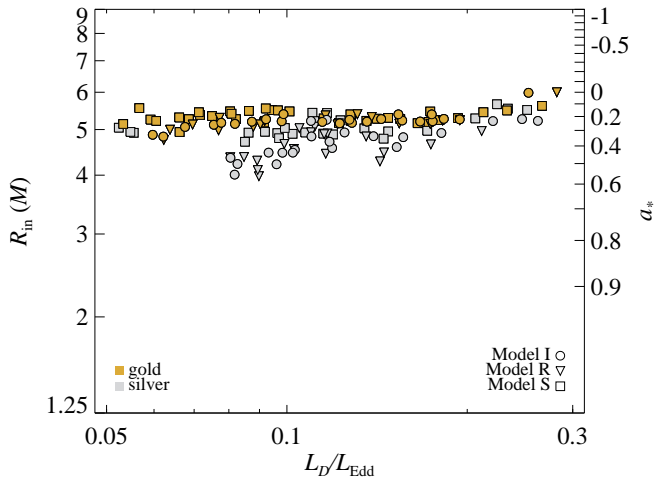


**Figure 3.** As in Figure 2, we again plot  $R_{\text{in}}$  and  $a_*$  versus luminosity, but we now show results for all three of the models discussed in the text. The data for Model S, which are repeated from Figure 2, show the highest degree of internal consistency.

In addition to the temperature/density limitations of REFLIONX just mentioned, this model has additional shortcomings. Of primary importance, it requires that the illuminating spectrum have a simple power law form. This power law is not truncated at low energies and its flux can rival or exceed the thermal flux, thereby leading to unphysical results (see e.g., Steiner et al. 2009). In addition, the strength of the reflected component is not linked to the normalisation of the illuminating spectrum, and so there is no way to ensure that the Compton and reflection components are appropriately matched. Nevertheless, we employ Model R using REFLIONX as a second-tier CF model that gives us an independent check on the results obtained using Model I.

In summary, using a variant of SIMPL and considering two reflection models, we have progressed toward a model featuring a self-consistent treatment of thermal disc emission, Compton scattering, and disc reflection. For estimating spin via the CF method, we favor IREFLECT, while for the Fe- $K\alpha$  method we elect to use REFLIONX and REFBHB (§ 6).

We now apply Model I (§ 4.2) to our set of *RXTE* spectra, while following the procedures described in § 3.2. In this case, we find that only a total of 45 spectra (24 *gold* and 21 *silver*) meet our selection criteria (§ 3.1), compared to the 60 selected using Model S. Our fitting results for these 45 spectra are given in Table 2.

For the *gold* spectra, we find excellent agreement between the results obtained using Model I,  $a_* = 0.23 \pm 0.06$ , and Model S,  $a_* = 0.20 \pm 0.04$ . This agreement is illustrated in Figure 3, where we also show results for Model R. As is apparent, considering only the *gold* spectra, all three models are in excellent agreement – the mean values of  $r_{\text{in}}$  are consistent with one another to within  $\approx 2$  per cent. However, for the *silver* spectra the mean values of  $r_{\text{in}}$  are depressed for all three models, by  $\approx 10$  per cent for the self-consistent reflection models (which track each other closely) and by only  $\approx 5$  per cent for Model S. Interestingly, the primitive Model S performs better than the self-consistent reflection models by harmonizing the results obtained from the two data sets and delivering the highest degree of internal consistency. Figure 4

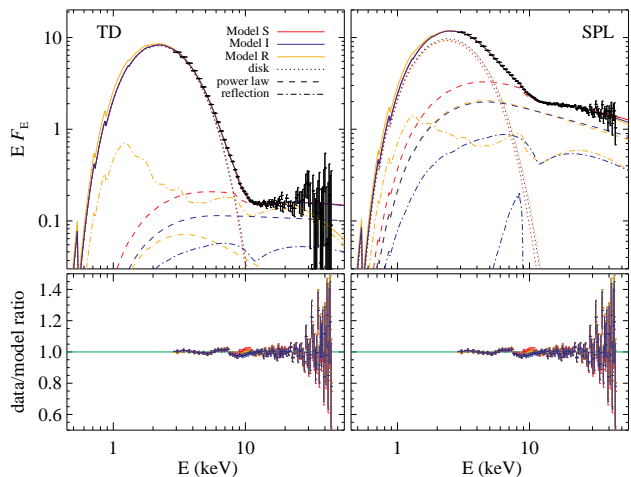


**Figure 4.** Model fits for a *gold* spectrum (left) and a *silver* spectrum (right), which correspond respectively to observations made on MJD 51121.0 and MJD 51115.3 (see Tabs. 1 & 2). The models are differentiated by line colour and the individual components by line texture. Note how much weaker the power-law component is for the *gold* spectrum, and how closely all three models track the data.

shows an overlay comparison of the best-fitting results using the three models for two representative spectra, one *gold* and the other *silver*. The total unfolded spectra and their components are plotted, as well as the data/model ratio. The key result of this section is that using our fiducial values of  $M$ ,  $i$  and  $D$  (§ 1), all three models applied to the *gold* spectra give the same low estimate of spin:  $0.15 < a_* < 0.35$ .

## 5 CONTINUUM FITTING: ERROR ANALYSIS AND FINAL SPIN RESULT

In this section, we broadly consider three sources of observational error, both systematic and statistical, which bear on our final estimate of the spin. In order of increasing importance, these are (1) sensitivity to the details of the spectral models employed; (2) X-ray flux calibration uncertainties; (3) and the uncertainties in the input parameters  $M$ ,  $i$  and  $D$ . We then perform a comprehensive analysis that incorporates these uncertainties and arrive at our final CF estimate of the spin of the black hole. In the following, we present an overview; for details, see Appendix A.

- *Sensitivity to X-ray spectral models.* In order to make this assessment, we determine the change in  $r_{\text{in}}$  when varying a single model component or a single one of the parameter settings. Table 3 gives the mean fractional change in  $r_{\text{in}}$  for the *gold* data sample that arises from changing either a model parameter (rows P1-9) or a model component (M1-5). The ‘Change’ column lists either the new value adopted for the parameter or it describes the change made to the model component (where DISC, PL, and REFL refer to the accretion disc, power law, and reflection components). The third and fourth columns respectively list the fractional changes in  $r_{\text{in}}$  for Model I and Model S. The largest tabulated uncertainty arises from the choice of the viscosity parameter: Using  $\alpha = 0.01$  instead of the default value ( $\alpha = 0.1$ ) de-

Table 2. Model I Continuum-Fitting Results

N	MJD	$\frac{L_D}{L_{\text{Edd}}}$	SIMPL-R		KERRBB2		IREFLECT	GAUSS	$\chi^2_{\nu}/\text{DOF}$	State
			$\Gamma$	$f_{sc}$	$a_*$	$\dot{M}(10^{18}\text{g/s})$	$\xi(\text{erg cm/s})$	$N(10^{-3}/\text{cm}^2/\text{s})$		
1	51117.4	0.18	2.04 ± 0.04	0.018 ± 0.002	0.235 ± 0.021	3.37 ± 0.11	1522 ± 1560	2.8 ± 2.7	0.7/74	TD
2	51119.0	0.16	2.07 ± 0.04	0.017 ± 0.002	0.230 ± 0.021	3.01 ± 0.09	1215 ± 1345	2.7 ± 2.0	0.7/74	TD
3	51121.0	0.14	2.06 ± 0.06	0.006 ± 0.001	0.238 ± 0.017	2.61 ± 0.07	1967 ± 2881	1.4 ± 1.1	0.7/74	TD
4	51124.7	0.11	2.07 ± 0.06	0.012 ± 0.002	0.240 ± 0.022	2.20 ± 0.07	1179 ± 2224	2.5 ± 1.5	0.6/74	TD
5	51128.6	0.10	2.09 ± 0.05	0.020 ± 0.003	0.236 ± 0.024	1.89 ± 0.07	1101 ± 1834	2.9 ± 1.5	0.9/74	TD
6	51130.5	0.09	2.15 ± 0.03	0.023 ± 0.001	0.221 ± 0.018	1.79 ± 0.05	311.1 ± 114.6	2.9 ± 0.9	1.1/74	TD
7	51132.5	0.08	2.07 ± 0.03	0.018 ± 0.001	0.254 ± 0.030	1.55 ± 0.07	1976 ± 1868	2.9 ± 1.2	0.8/74	TD
8	51134.5	0.08	2.15 ± 0.04	0.013 ± 0.001	0.261 ± 0.028	1.43 ± 0.06	1935 ± 2203	1.9 ± 0.8	0.8/74	TD
9	51136.9	0.07	2.08 ± 0.21	0.013 ± 0.008	0.276 ± 0.031	1.26 ± 0.07	732.7 ± 5296	2.0 ± 1.0	0.9/74	TD
10	51157.6	0.12	2.63 ± 0.70	0.004 ± 0.007	0.251 ± 0.020	2.33 ± 0.08	606.7 ± 10500	0.5 ± 0.8	0.8/74	TD
11	51160.3	0.17	1.97 ± 0.32	0.001 ± 0.001	0.237 ± 0.017	3.21 ± 0.08	50600 ± 741400	0.0 ± 1.5	0.7/74	TD
12	51163.2	0.25	2.66 ± 1.29	0.001 ± 0.003	0.005 ± 0.028	5.62 ± 0.17	10 ± 3988	3.4 ± 3.0	1.7/74	TD
13	51260.6	0.19	1.97 ± 0.04	0.015 ± 0.001	0.222 ± 0.021	3.77 ± 0.11	5823 ± 4795	4.5 ± 3.0	0.4/66	TD
14	51261.8	0.18	2.04 ± 0.04	0.018 ± 0.002	0.218 ± 0.022	3.56 ± 0.12	1527 ± 1575	2.4 ± 2.9	0.7/66	TD
15	51263.1	0.17	2.07 ± 0.04	0.020 ± 0.002	0.184 ± 0.034	3.48 ± 0.15	1869 ± 1752	4.7 ± 3.0	0.5/66	TD
16	51264.8	0.15	1.97 ± 0.03	0.014 ± 0.001	0.184 ± 0.032	3.06 ± 0.12	5574 ± 3975	7.2 ± 1.9	0.8/66	TD
17	51265.6	0.14	2.10 ± 0.08	0.022 ± 0.004	0.219 ± 0.020	2.79 ± 0.09	547 ± 1228	3.3 ± 1.5	0.7/66	TD
18	51266.9	0.13	2.08 ± 0.23	0.014 ± 0.008	0.247 ± 0.027	2.45 ± 0.12	672.7 ± 4994	2.6 ± 2.0	0.5/66	TD
19	51267.6	0.13	2.08 ± 0.17	0.022 ± 0.009	0.225 ± 0.027	2.47 ± 0.13	697.8 ± 3756	4.9 ± 2.6	0.8/66	TD
20	51273.6	0.10	1.95 ± 0.03	0.015 ± 0.001	0.183 ± 0.040	1.97 ± 0.10	10000 ± 8847	8.1 ± 1.4	1.9/66	TD
21	51274.5	0.09	2.04 ± 0.10	0.018 ± 0.005	0.238 ± 0.028	1.68 ± 0.08	827.3 ± 2862	3.1 ± 1.6	0.8/66	TD
22	51276.3	0.08	1.99 ± 0.19	0.010 ± 0.004	0.246 ± 0.028	1.48 ± 0.07	516.7 ± 2565	2.6 ± 0.7	0.7/66	TD
23	51278.7	0.06	1.92 ± 0.06	0.011 ± 0.001	0.341 ± 0.031	1.11 ± 0.06	23140 ± 53800	3.6 ± 1.2	0.8/66	TD
24	51279.6	0.06	1.99 ± 0.31	0.013 ± 0.011	0.329 ± 0.022	1.07 ± 0.05	677.9 ± 7036	2.1 ± 1.1	0.8/66	TD
25	51110.3	0.26	2.45 ± 0.02	0.109 ± 0.005	0.233 ± 0.033	5.06 ± 0.20	4879 ± 2066	16.8 ± 9.5	0.8/74	INT
26	51111.6	0.25	2.39 ± 0.03	0.113 ± 0.006	0.220 ± 0.040	4.80 ± 0.23	7147 ± 4072	24.1 ± 11.0	0.7/74	INT
27	51113.7	0.22	2.43 ± 0.03	0.108 ± 0.007	0.234 ± 0.045	4.25 ± 0.24	2331 ± 1531	16.7 ± 9.4	0.9/74	INT
28	51115.3	0.18	2.39 ± 0.07	0.086 ± 0.011	0.317 ± 0.041	3.28 ± 0.26	875.9 ± 1712	9.0 ± 6.9	0.7/74	SPL
29	51126.6	0.11	2.14 ± 0.03	0.025 ± 0.001	0.233 ± 0.024	2.11 ± 0.08	10000 ± 6716	8.8 ± 1.7	1.5/74	INT
30	51269.7	0.12	2.10 ± 0.03	0.022 ± 0.001	0.225 ± 0.025	2.26 ± 0.08	10000 ± 8200	9.1 ± 1.9	1.4/66	SPL
31	51270.8	0.08	2.17 ± 0.03	0.053 ± 0.003	0.502 ± 0.025	1.28 ± 0.06	10000 ± 6763	10.2 ± 2.5	1.6/66	SPL
32	51271.4	0.08	2.20 ± 0.03	0.059 ± 0.003	0.469 ± 0.044	1.29 ± 0.10	10000 ± 7370	9.5 ± 3.0	1.2/66	SPL
33	51664.4	0.16	2.40 ± 0.04	0.090 ± 0.005	0.345 ± 0.029	2.78 ± 0.12	511.2 ± 558.9	10.2 ± 3.5	0.6/66	SPL
34	51664.7	0.15	2.40 ± 0.05	0.097 ± 0.007	0.407 ± 0.024	2.58 ± 0.13	568.4 ± 836.3	10.4 ± 3.8	0.9/66	SPL
35	51665.4	0.14	2.37 ± 0.13	0.079 ± 0.019	0.339 ± 0.055	2.49 ± 0.31	745.6 ± 3070	7.6 ± 6.3	0.6/66	SPL
36	51667.7	0.12	2.29 ± 0.03	0.067 ± 0.005	0.412 ± 0.029	2.00 ± 0.11	1533 ± 1302	8.3 ± 3.9	0.7/66	SPL
37	51668.8	0.12	2.32 ± 0.04	0.068 ± 0.005	0.374 ± 0.034	2.04 ± 0.11	515.3 ± 602.9	6.2 ± 2.1	0.8/66	SPL
38	51669.2	0.12	2.35 ± 0.02	0.063 ± 0.002	0.314 ± 0.023	2.27 ± 0.08	232.8 ± 91.73	7.6 ± 2.5	0.9/66	SPL
39	51670.6	0.10	2.30 ± 0.03	0.079 ± 0.004	0.423 ± 0.023	1.72 ± 0.07	455.3 ± 353.1	8.0 ± 2.3	0.7/66	SPL
40	51670.8	0.10	2.25 ± 0.03	0.060 ± 0.004	0.439 ± 0.030	1.68 ± 0.09	1661 ± 1319	7.2 ± 3.2	0.7/66	INT
41	51671.4	0.11	2.29 ± 0.13	0.058 ± 0.016	0.340 ± 0.036	1.96 ± 0.17	646.3 ± 2684	7.3 ± 2.5	0.9/66	SPL
42	51672.4	0.09	2.25 ± 0.10	0.067 ± 0.014	0.439 ± 0.040	1.53 ± 0.15	818.8 ± 2652	7.4 ± 4.4	0.7/66	SPL
43	51673.0	0.10	2.33 ± 0.07	0.109 ± 0.013	0.504 ± 0.045	1.49 ± 0.16	947.3 ± 1858	10.1 ± 5.7	0.6/66	INT
44	51673.4	0.10	2.36 ± 0.09	0.103 ± 0.017	0.440 ± 0.060	1.61 ± 0.23	860.7 ± 2522	10.1 ± 6.1	0.8/66	INT
45	51674.7	0.08	2.22 ± 0.03	0.113 ± 0.006	0.556 ± 0.046	1.20 ± 0.11	2605 ± 1802	11.3 ± 5.6	0.6/66	INT

Note. —

<sup>1</sup> Reported error estimates are symmetric  $1\sigma$  statistical uncertainties.<sup>2</sup>  $M$ ,  $i$ , and  $D$  are frozen at their fiducial values.

creases  $r_{\text{in}}$  by  $\approx 6$  per cent for Model I and 3 per cent for Model S. Each of the other 13 changes considered affect  $r_{\text{in}}$  by  $< 3$  per cent for either model.



• *Flux calibration.* The problem of flux calibration is endemic to X-ray astronomy. The Crab spectrum, as determined by Toor & Seward (1974), is the widely-adopted standard that we have consistently used in our work. Uncertainties in the normalisation of this spectrum have recently been considered by Weisskopf et al. (2010). Using their Figure 1 as a guide, we adopt a generous  $\pm 10$  per cent uncertainty in our overall flux calibration, which corresponds to a 5 per cent uncertainty in  $r_{\text{in}}$ .

• *Uncertainties in  $M$ ,  $i$  and  $D$ .* As in our earlier work (e.g., Liu et al. 2008; Gou et al. 2009, 2010), we sample the allowed parameter space assuming Gaussian errors (except here for  $D$ , we use an asymmetric Gaussian). The sampling is performed using 42,500 triplets of  $M$ ,  $i$ , and  $D$ , which are distributed in a uniform grid throughout the parameter space. At each point in the grid, the complete *RXTE* data set is analysed with Model S, and the selection criteria given in § 3 are separately applied to the results. Folding all of the runs together, a composite distribution based on all of the selected spectra is obtained, where we have additionally weighted over the set of possible dynamical models (see Table 1 in Orosz et al. 2010).

In conducting this analysis, we have included the robust no-eclipse constraint,  $i < 82^\circ$ . We have further required that during the TD-state plateau phase (days 105–182; Figure 1) the disc luminosity not exceed 85 per cent of  $L_{\text{Edd}}$  (the actual Eddington limit for disc geometry; see Section 6.1 in McClintock et al. 2006). Lastly, we also require that the disc luminosity during the thermal plateau phase be greater than 10 per cent of  $L_{\text{Edd}}$ , or else the full sample of TD data would extend downward in luminosity to the unreasonably low value of  $\lesssim 0.1$  per cent  $L_{\text{Edd}}$ .

In the analysis described above, we have used the default value of the viscosity parameter,  $\alpha = 0.1$ . Because  $\alpha$  is the major source of uncertainty considered in Table 3, we have repeated the analysis just described using  $\alpha = 0.01$  and combined the two distributions, weighting them equally. We combine all other errors in Table 3, yielding an ensemble value of  $\approx 4.2$  per cent. Finally, we add in quadrature the 5 per cent error in the absolute flux calibration and arrive at our net error of 6.5 per cent. The effect of this uncertainty on our measurement of spin is incorporated by running a box-car smoothing kernel (with a 13 per cent full width) over the distribution for  $r_{\text{in}}$ .

The dominant source of error is the observational uncertainties in  $M$ ,  $i$  and  $D$ , which in turn are largely due to the uncertainties associated with modeling the optical/NIR light curves (Orosz et al. 2010). Figure 5 shows the dependence of  $r_{\text{in}}/\text{spin}$  on these model parameters. Here, using the results of the grid analysis described above, we vary one of the three parameters, fixing the other two at their best values. The strong correlations between spin and inclination, and between spin and distance, demonstrate the degree to which measurement errors in these quantities contribute to the uncertainty in spin. Together, errors in  $M$ ,  $i$ , and  $D$  account for  $\Delta a_* \approx 0.25$  ( $\Delta r_{\text{in}}/r_{\text{in}} \approx 0.2$ ) for the 90 per cent confidence interval. The contribution due to the inclination is sizable,  $\sim 11$  per cent, because its uncertainty and its value are large ( $\lesssim 4$  degrees and 74.7 degrees, respectively). The uncertainty in  $D$  likewise contributes  $\sim 11$

**Table 3.** Systematic Changes to the Model

TD	Change	$\Delta \bar{r}_{\text{in}} (\%)$	
		Model I	Model S
P1	$\alpha = 0.01$	-5.98	-2.90
P2	$N_{\text{H}} = 6 \times 10^{21} \text{ cm}^{-2}$	-2.90	-1.94
P3	$N_{\text{H}} = 10 \times 10^{21} \text{ cm}^{-2}$	0.84	2.84
P4	$x = 1.5$	-1.13	...
P5	$x = 1.1$	-1.26	...
P6	$q$ and $x$ free	0.21	...
P7	$T_{\text{disk}} = 10^6 \text{ K}$	-0.09	...
P8	$W_{\text{Edge}} = 3.5 \text{ keV}$	...	-0.42
P9	$W_{\text{Edge}} = 14 \text{ keV}$	...	0.41
M1	DISK: BHSPEC	1.30	2.88
M2	PL: falloff with $kT_e$	-1.53	-0.66
M3	PL: down-scattering set	-0.27	0.07
M4	REFL: SMEDGE	1.70	...
M5	REFL: REFLIONX	-1.00	-2.65

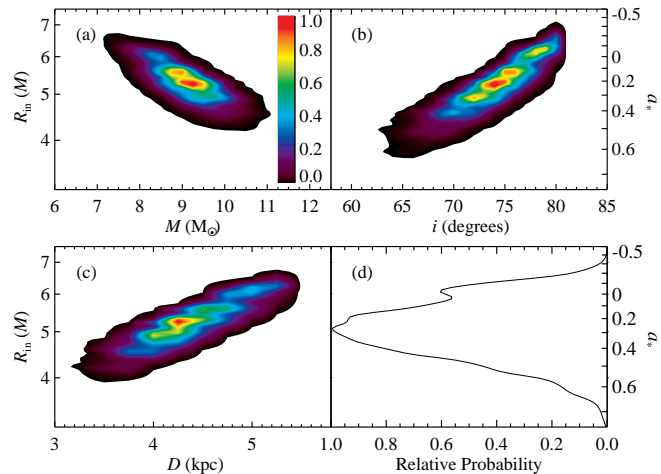


**Figure 5.** Probability contours for the relationship between  $r_{\text{in}}/\text{spin}$  and  $M$ ,  $i$ , and  $D$ . Each of the first three panels (a–c) shows variation for a single parameter; the other two parameters have been fixed at their best values. The orientations of the probability ellipsoids show that spin is positively correlated with  $M$  and negatively correlated with both  $i$  and  $D$ . In panel (d), a combined probability distribution for the case  $\alpha = 0.1$  is shown (arbitrarily scaled) with variation in  $M$ ,  $i$ , and  $D$  folded together.

per cent, while uncertainties in the mass affect the spin only at the  $\sim 7$  per cent level.

After folding together all sources of error, the resulting probability distribution is shown in Figure 6, with  $R_{\text{in}}$  and  $a_*$  displayed respectively on the bottom and top axes. The green vertical line identifies the most probable spin,  $a_* = 0.34$ , and the yellow lines indicate the 90 per cent confidence interval, which extends from -0.11 to 0.71. From an inspection of this distribution function, we conclude that the black hole is unlikely to be in a retrograde configuration (only  $\sim 11.2$  per cent probability). Of greater importance, we conclude that *the spin is not high*. For example, the probability that the CF spin exceeds 0.9 is less than 0.4 per cent,

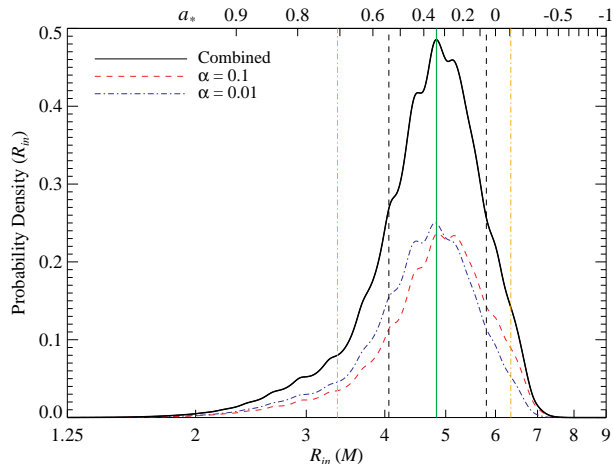


**Figure 6.** Composite probability density for  $R_{\text{in}}$  and  $a_*$  which takes into account both systematic and statistical errors including: uncertainties in distance, black hole mass and inclination; the spectral model; and the uncertainty in the absolute flux calibration. The net probability distribution is a combination of the individual distributions for two values of  $\alpha$ . The contribution from each integrates to 50 per cent probability and is shown for  $\alpha = 0.01$  (blue dash-dotted line) and  $\alpha = 0.1$  (red dashed line). The 90 per cent confidence limits for the combined distribution are shown as yellow vertical lines, the  $1\sigma$  limits as vertical black lines, and the most probable spin is marked with a green line. We conclude that the spin is moderate:  $-0.11 < a_* < 0.71$  (90 per cent confidence).

a surprising result for a black hole that has produced superluminal jets.

## 6 SPIN FROM REFLECTION FEATURES

In the previous section, we concluded that the spin parameter has a low or intermediate value. This result is based on our CF analysis of many *RXTE* spectra, which were obtained primarily in the TD state. In what follows, we first analyse intermediate-state spectra of J1550 obtained with the *ASCA* X-ray observatory; we then supplement this analysis using a sample of *RXTE* spectra, also obtained in the intermediate state. We fit the *ASCA* GIS-2 and GIS-3 data simultaneously, using a floating normalisation constant to allow for cross-calibration uncertainties. Our work differs from earlier analyses of these same data by others (e.g., see Miller et al. 2005; Gierliński & Done 2003; Miller et al. 2009): Our focus is on a detailed analysis of the reflection component, rather than on a precise model of the overall continuum. We begin by setting all the physical parameters of the binary to the best-estimate values presented in Orosz et al. (2010).

In addition to the soft disc and hard power-law components seen in the TD- and intermediate-state spectra of black hole binaries, a broad emission line at  $\sim 6.4$  keV is also often present (see e.g. Miller 2007). This line feature is merely the most prominent reflection signature that arises as hard emission from the corona irradiates the cooler disc (Ross & Fabian 2005). In the vicinity of a black hole, the iron- $K\alpha$  line shape and other reflection features are distorted by various relativistic effects (Fabian et al. 1989; Laor

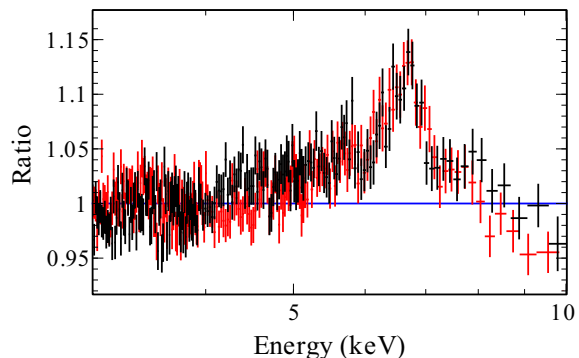


**Figure 7.** Data/model ratio for a phenomenological continuum model consisting of a thermal disc and a Compton component. *ASCA* GIS-2 and GIS-3 spectra are shown in black and red respectively. The data were fitted jointly in the 1–4 and 7–10 keV energy range. The residuals in the 4–7 keV band show the relativistic nature (asymmetry and broadness) of the iron-emission line profile. The data have been rebinned for plotting purposes. The data/model ratio for the full energy range is shown in Fig. 8.

1991). The spin parameter can be constrained by modeling these features because their shape depends on how far the disc extends down into the gravitational potential well (see § 1), the key assumption again being that this extent is set by the radius of the ISCO.

### 6.1 Phenomenological Models – *ASCA*

In order to highlight the relativistic nature of the line profile in the *ASCA* spectra, we start by modeling the 1–4 keV and 7–10 keV continua with a combination of a disc blackbody (described by the XSPEC model DISKBB<sup>3</sup> of Mitsuda et al. 1984) and the Comptonisation model SIMPL. The neutral hydrogen column was initially fixed at  $N_{\text{H}} = 8 \times 10^{21} \text{ cm}^{-2}$  as per Miller et al. (2003), which resulted in a poor fit to the continuum with  $\chi^2/\nu = 2172.3/1002$ . Allowing the column density to vary resulted in a significant improvement to the fit with  $\chi^2/\nu = 1367.5/1001$  for  $N_{\text{H}} = 5.4 \pm 0.1 \times 10^{21} \text{ cm}^{-2}$ . The total neutral hydrogen column density in the line of sight to J1550, which was determined using the *Chandra* transmission grating, is not expected to vary (Miller, Cackett & Reis 2009). However, the differing values of  $N_{\text{H}}$  can be reasonably attributed to differences in the calibrations of the *Chandra* and *ASCA* detectors. Furthermore, allowing  $N_{\text{H}}$  to differ between the two GIS spectra further improves the fit:  $\Delta\chi^2 = -47.5$  for one less degree of freedom with a difference in  $N_{\text{H}}$  of  $< 5$  per cent. Figure 7 shows the line spectrum obtained by modeling the continuum as described above. The asymmetric and broad residual feature in the 4–7 keV band has the appearance one expects for fluorescent disc-line emission arising near a black hole.

<sup>3</sup> This model characterises the thermal emission using only two parameters – the flux normalisation and a colour temperature. Here, we use this very approximate model of the continuum (compare § 3) because of its simplicity in *phenomenologically* describing the thermal continuum.

We provide a physical description of the Fe line by first modeling the residuals seen in Figure 7 using the LAOR model (Laor 1991) and fitting for the inner radius  $r_{\text{in}}$  and the power-law index  $q$  of the emissivity profile, which is described by a power-law of the form  $\epsilon(r) \propto r^{-q}$ . The outer disc radius is fixed at the maximum allowed value of  $400 r_{\text{g}}$  ( $r_{\text{g}} \equiv GM/c^2$ ), and the disc inclination is constrained to be approximately  $1\sigma$  from the adopted value of Orosz et al. (2010) (i.e. between 71 and 78 degrees). The line energy is constrained between 6.4–6.97 keV. The fit achieved by including the LAOR component, shown in Figure 8, results in  $\chi^2/\nu = 1848.0/1501$ , an improvement of  $\Delta\chi^2 = -416$  for 5 fewer degrees of freedom (compared to the best-fitting continuum model with no line feature). The best fit parameters for this model are detailed in Table 4 (Model 1).

It can be seen from the ratio plot shown in Figure 8 that this simple, heuristic model, although mostly adequate, does not provide a detailed description of all the features present in the 6–8 keV range. Adding a narrow Gaussian line at  $\approx 6.7$  keV only marginally improves the fit<sup>4</sup> ( $\Delta\chi^2 = -14.4$  for 2 fewer degrees of freedom), with evidence for additional residuals, which are possibly associated with Fe-K-shell absorption edges in partially ionised material (Ross & Fabian 1993; Ross et al. 1996). Such features are usually present at  $\approx 7.1$  keV in TD-state spectra of black hole binaries (Done et al. 1992; Reis et al. 2008). In order to properly account for the panorama of features associated with the re-processing of radiation in the accretion disc, we now consider complete reflection models.

## 6.2 Reflection Analysis – ASCA

We replace the LAOR component with REFLIONX (Ross & Fabian 2005), which describes the spectrum reflected from an optically-thick and cold atmosphere of constant density that is illuminated by a power-law spectrum (§ 4). The parameters of the model are the iron abundance (set to Solar), photon index of the illuminating power law, ionisation parameter, and normalisation. The gravitational and Doppler effects are accounted for using the fully relativistic convolution model KERRCONV (Brenneman & Reynolds 2006), which includes black hole spin as a fit parameter. The power-law indexes of REFLIONX and the Compton component (SIMPL-R) are tied, and, as before, we constrain the inclination to lie between 71 and 78 degrees and include a narrow Gaussian line at  $\approx 6.7$  keV. The model results in a good and improved fit to the data with  $\chi^2/\nu = 1752.3/1499$  (Model 2 in Table 4); however it still does not fully account for the reflection features, with residuals present at  $\approx 7$  keV (top panel of Fig. 9).

Although the scattered fraction for this spectrum is high,  $f_{\text{SC}} > 50$  per cent, and the CF method is not applicable, we nevertheless investigated the effect of switching the continuum model from DISKBB to KERRBB (Model 3), with the mass, distance and inclination frozen at their nominal values. This change produced insignificant differences in the fit parameters (Table 4). For both Models 2 and 3, we

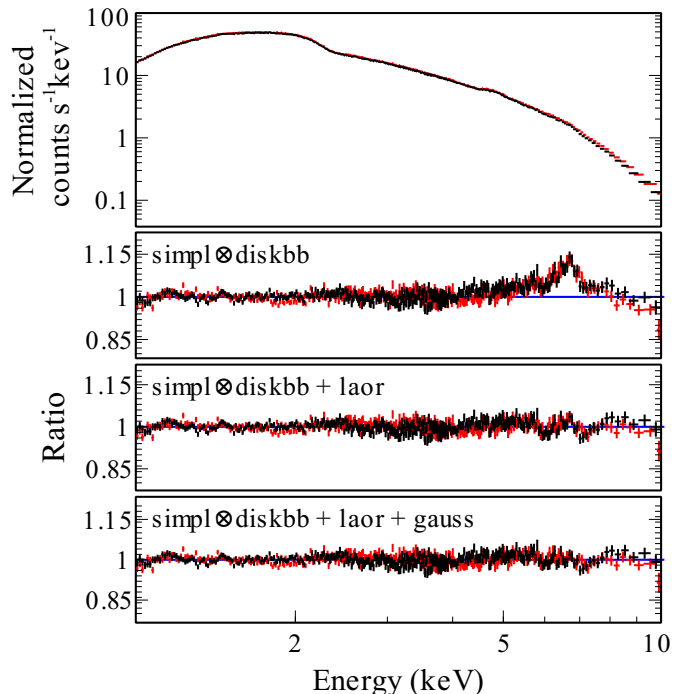


**Figure 8.** (*top:*) The ASCA spectra. Below are plots of the ratio of the data to a phenomenological continuum model consisting of thermal-disc and Compton components plus a LAOR line; in the bottommost panel, a narrow Gaussian line has been added to the model.

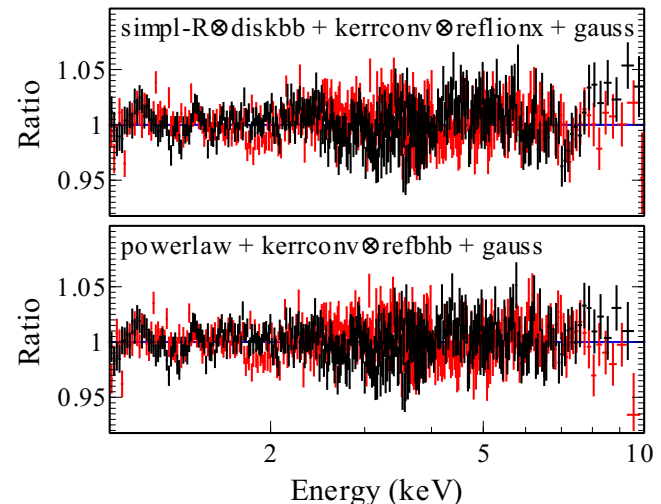


**Figure 9.** Data/model ratio for (*top:*) the REFLIONX model together with a separate thermal emission and Compton component. (*bottom:*) Self-consistent thermal emission and reflection (REFBHB) together with a power-law component.

find that the spin parameter is moderate ( $< 0.75$ ). Meanwhile, the disc ionisation has pegged at its maximum value ( $\xi = 10^4 \text{ erg cm}^{-2} \text{ s}^{-1}$ ) indicating that the surface layer of the accretion disc is highly ionised, with iron possibly being fully ionised. In such circumstances, the Fe absorption edge can be particularly strong and is often found to be highly smeared (see Ross et al. 1996 and references therein).

In order to incorporate the effects of thermal ionisation

<sup>4</sup> This feature was previously associated (Tomsick et al. 2001) with emission from the Galactic ridge (Valinia & Marshall 1998).

**Table 4.** *ASCA* 1-10 keV spectral fit parameters with a variety of reflection-based models.

Parameters	Model 1	Model 2	Model 3	Model 4	Model 5
	SIMPL-R⊗DISKBB +LAOR	SIMPL-R⊗DISKBB +KERRCONV⊗REFLIONX	SIMPL-R⊗KERRBB +KERRCONV⊗REFLIONX	POWERLAW +KERRCONV⊗REFBHB	
$N_{\text{H}}$ ( $\times 10^{22}$ cm $^{-2}$ )	$0.576^{+0.003}_{-0.002}$	$0.650^{+0.006}_{-0.002}$	$0.666^{+0.002}_{-0.007}$	$0.663^{+0.002}_{-0.006}$	$0.653^{+0.009}_{-0.007}$
$\Gamma$	$2.40 \pm 0.01$	$2.329^{+0.006}_{-0.010}$	$2.320^{+0.003}_{-0.002}$	$2.24 \pm 0.01$	$2.22^{+0.03}_{-0.02}$
$f_{\text{SC}} (N_{\text{hard}})^a$	$0.6 \pm 0.3$	$0.64 \pm 0.04$	$0.616 \pm 0.002$	$2.4 \pm 0.1$	$2.3^{+0.2}_{-0.1}$
$kT$ (keV)	$0.513^{+0.009}_{-0.006}$	$0.566^{+0.001}_{-0.013}$	—	$0.540 \pm 0.001$	$0.542^{+0.002}_{-0.001}$
$N_{\text{diskbb}}$ ( $(\frac{R}{D/10 \text{ kpc}})^2 \cos i$ )	$5200^{+500}_{-200}$	$4211^{+86}_{-272}$	—	—	—
$\dot{M}$ ( $\times 10^{18}$ g s $^{-1}$ )	—	—	$0.668^{+0.003}_{-0.03}$	—	—
$q$	$2.0 \pm 0.2$	$1.88 \pm 0.01$	$1.85^{+0.2}_{-0.30}$	$2.38^{+0.04}_{-0.07}$	$2.5^{+0.2}_{-0.1}$
$i$ (degrees)	71–78	71–78	71–78	$77 \pm 1$	$82_{-3}$
$E_{\text{Laor}}$ (keV)	$6.40^{+0.01}$	—	—	—	—
$r_{\text{in}}$ ( $r_{\text{g}}$ )	$8.2^{+2.9}_{-3.5}$	—	—	—	—
$N_{\text{laor}}$ ( $\times 10^{-3}$ )	$7.1 \pm 0.1$	—	—	—	—
$\xi$ (erg cm s $^{-1}$ )	—	$10000_{-320}$	$10000_{-900}$	—	—
$N_{\text{reflionx}}$ ( $\times 10^{-6}$ )	—	$1.32 \pm 0.06$	$1.288^{+0.004}_{-0.070}$	—	—
$H_{\text{den}}$ ( $\times 10^{22}$ H cm $^{-3}$ )	—	—	—	$1.00_{-0.02}$	$1.00_{-0.02}$
$F_{\text{illum}}/F_{\text{bb}}$	—	—	—	$0.29^{+0.03}_{-0.18}$	$0.25^{+0.08}_{-0.07}$
$N_{\text{refbhb}}$ ( $\times 10^{-2}$ )	—	—	—	$6.2^{+0.2}_{-2.7}$	$5.96^{+0.5}_{-1.1}$
spin ( $a_*$ )	—	$< 0.75$	$0.45 (< 0.75)$	$0.6 (> 0.38)$	$0.55^{+0.15}_{-0.22}$
$\chi^2/\nu$	1848.0/1501	1752.3/1499	1759.5/1499	1700.9/1498	1698.6/1498

Notes: All errors are quoted at the 90 per cent confidence level for one parameter of interest  $\Delta\chi^2 = 2.71$ ). Model 1, which is purely phenomenological, uses the familiar LAOR line and allows a comparison with previous work. Models 2 and 3 use different disc components; however both of them employ the same full reflection model (REFLIONX), while treating the Compton component using SIMPL-R (§ 4.1). The core of Model 4 is REFBHB which is likewise a full reflection model, with the added virtue that it self-consistently models the thermal component as well. In Models 1 to 4 the inclination was constrained to be between 71 and 78 degrees. In Model 5 the inclination is allowed to range from 60 to 82 degrees. A constraint on the inclination was achieved only for Models 4 and 5.

<sup>a</sup> The POWERLAW normalisation is in photons cm $^{-2}$  s $^{-1}$  for Models 4 and 5. For Models 1–3, the normalisation is given by the dimensionless parameter  $f_{\text{SC}}$  (see § 3).

expected for a hot accretion disc, we replace REFLIONX with the model REFBHB developed by Ross & Fabian (2007). This reflection model accounts for both thermal X-ray emission and the reflection features. The effects of Compton broadening in the disc are fully included, subject to the one assumption of a constant-density atmosphere. The parameters of the model are the number density of hydrogen in the illuminated surface layer,  $H_{\text{den}}$ , the temperature of the blackbody heating the surface layers, the power-law photon index, and the ratio of the total flux illuminating the disc to the total blackbody flux emitted by the disc. Again, we tie the power-law index of REFBHB to that of the Compton component – now modelled as a standard power law – and convolve the spectrum with KERRCONV in order to include relativistic broadening. The model results in an excellent fit to the data with  $\chi^2/\nu = 1700.9/1498$  (Model 4, see bottom panel in Fig. 9), however the hydrogen surface density is pegged at the maximum value of the model. The ionisation state of the disc is inversely proportional to the value of the hydrogen density and thus the pegged value implies that the fit is requiring a higher amount of emission in the form of discrete features as opposed to the near featureless reflected continuum arising from a highly ionised disc-surface. A similar result would be produced by increasing the iron abundance. Unfortunately the model in its current format does not allow for a change in elemental abundances. In order to investigate the effect that  $H_{\text{den}}$  has on the spin parameter

we fixed it at  $1 \times 10^{21}$  H cm $^{-3}$  using Model 4 (i.e. an order of magnitude less than the value presented in Table 4) and refitted the data. This constraint on  $H_{\text{den}}$  resulted in an adequate fit with  $\chi^2/\nu = 1731.6/1499$  and a spin value of  $0.60 \pm 0.05$ . We note here that POWERLAW has been used to model the Compton component. We have explored replacing POWERLAW with SIMPL-R, and the fit becomes worse with  $\chi^2/\nu = 1802.5/1498$ . However, the value of the spin parameter, as well as those of the reflection parameters, remains largely unchanged.

From Models 1 to 4 it is clear that the spin parameter is consistently below  $\approx 0.75$ . However, in the first three cases inclination is not constrained. For this reason we explore a very broad range of  $i$ , from  $60^\circ$  to  $82^\circ$ . We note that above this limit, the disc would be super-Eddington during its steady thermal plateau in Figure 1. The best fit is given by Model 5 (Tab. 4) and reaches the upper inclination limit, netting a small improvement ( $\Delta\chi^2 = -2.3$ ) over Model 4. For all models we see that the emissivity index is consistently below the typical value of three associated with the canonical ‘lamp-post’ coronal geometry, and is instead more consistent with a slab-like corona. In order to illuminate any degeneracy between the value of spin and either the emissivity index or inclination, we show in Figure 10 the 68, 90 and 95 per cent probability contours for these parameters plotted versus spin. In both instances there exists a small and negative correlation with spin. However it is

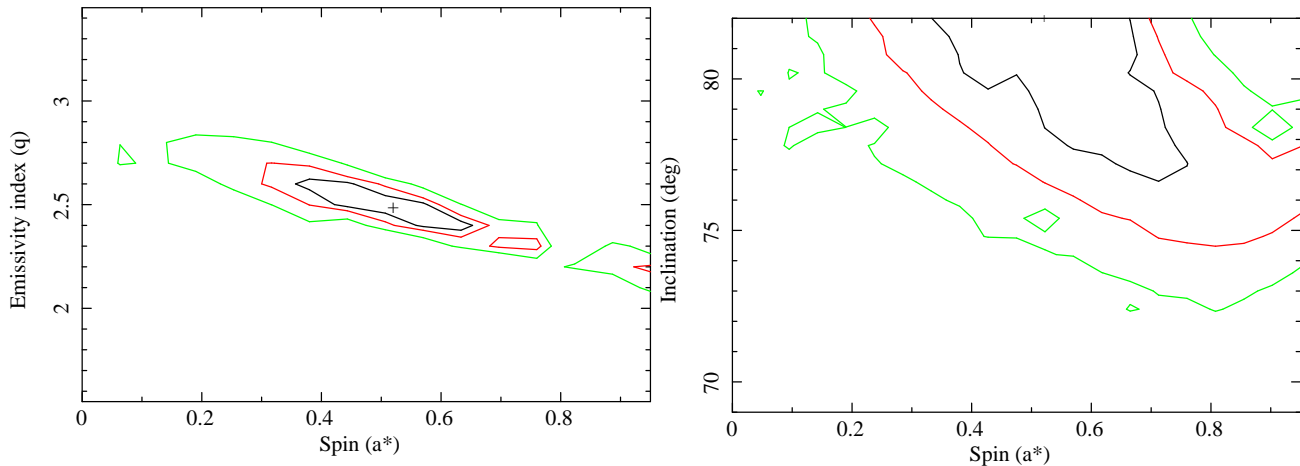


**Figure 10.** (left): Emissivity versus spin contour plot for J1550. The 68, 90 and 95 per cent confidence range for two parameters of interest are shown in black, red and green, respectively. We have allowed  $i$  to take any value between  $60 \leq i \leq 82$ , and find that the spin is greater than 0.33 at the 90 per cent level of confidence. (right): Similar plot for inclination versus spin. We see from the *ASCA* data that a zero spin value is clearly ruled out, as is an inclination lower than  $72^\circ$ .

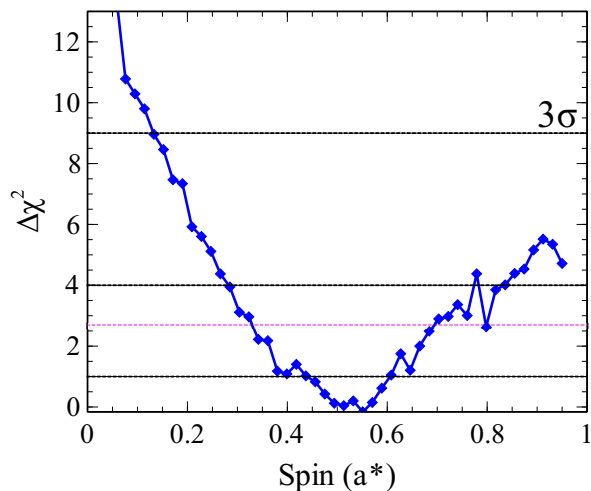


**Figure 11.** Goodness-of-fit versus spin parameter for J1550. From the reflection features present in the *ASCA* spectra of J1550 we can rule out a non rotating black hole at over  $3\sigma$  confidence. However we cannot place a comparable strong upper limit on this value. The 90 per cent confidence level ( $\Delta\chi^2 = 2.71$  for one parameter of interest) is shown in magenta. The black dotted lines indicate confidence intervals. Spin is constrained to  $0.33 < a_* < 0.70$  at the 90 per cent confidence level.

also clear that  $q$  is well constrained between 2.2 and 2.7 and that  $i \gtrsim 75^\circ$  at 90 per cent confidence even while including the uncertainty in spin. When we marginalize over these parameters and compute the uncertainty in spin alone (Figure 11 for Model 5), the spin parameter obtained from the gravitational blurring of reflection features is constrained to be in the window  $0.33 < a_* < 0.70$  at 90 per cent confidence with the best estimate at  $a_* \approx 0.55$ . A non-rotating Schwarzschild black hole is rejected at greater than  $3\sigma$ .

Our measured spin using the REFBHB model is consistently lower than the preliminary value of  $a_* = 0.75 - 0.80$  reported by Miller et al. (2009), and we have attained a bet-

ter fit than they ( $\Delta\chi^2 \lesssim -100$ ) for more degrees of freedom. The critical difference in our model and spin estimate comes from having incorporated the effect Compton-broadening of the iron  $K\alpha$  line in the hot layers of the accretion disc. With REFBHB the disc is intrinsically hot and therefore the effect of Compton-broadening is fully accounted for when modeling the data. The extra broadening caused by this effect acts to lower the degree of gravitational broadening and as such requires less extreme spin parameters as compared with models where the reflection is assumed to come from a relatively cold surface, e.g, for AGN (Ross & Fabian 2007). This behavior can indeed be appreciated when we compare the spin value obtained from REFLIONX – a reflection model specifically designed for a cold accretion disc – to that of REFBHB. We see from Table 4 that for Models 2 and 3 the spin cover a higher range, with the 90 per cent error going as high as 0.75.

### 6.3 Spin from reflection features – *RXTE*

In order to supplement the *ASCA* spin measurement above, we present an analysis of a sample of ten *RXTE* spectra selected from the composite data set discussed in §§ 3,4 to have the following properties: very large scattered fraction,  $f_{\text{SC}} > 50$  per cent, goodness of fit,  $\chi^2/\nu < 2$ , and uniform values of luminosity and photon index,  $L_{\text{D}}/L_{\text{Edd}} \approx 0.2 \pm 0.05$  and  $\Gamma \approx 2.5 \pm 0.1$ , respectively. We begin by simultaneously modeling the reflection features present in all the *RXTE* spectra using REFLIONX convolved with KERRCONV while using SIMPL-R $\otimes$ DISKBB for the thermal plus Compton continuum (Model 2 in § 6.2). (N.B. The REFBHB component used in Models 4 and 5 was unable to converge to an adequate fit for *RXTE* and provided no spin constraint. Therefore, in this section we adopt Model 2.) The spin, in-

clination ( $60 \leq i \leq 82$ ) and emissivity index<sup>5</sup> are treated as global parameters among the ten spectra. As in § 3, the neutral hydrogen column density is fixed at  $8 \times 10^{21} \text{ cm}^{-2}$ . The remaining parameters were allowed to vary in individual spectra. Figure 12 shows the best-fitting model spectra (top panel) together with the data-to-model ratio for each spectrum (bottom panel). The fit was marginally improved ( $\Delta\chi^2 = -30.5$  for 10 degrees of freedom) by including a narrow line at  $\approx 6.7 \text{ keV}$  which accounts for the slight curvature in the residuals at that energy (compare the lower two panels in Fig. 12).

We find that the global best fit is sensitive to the upper energy range adopted for the *RXTE* spectra, which we attribute in part to a competition between the lower energy reflection features and the high-energy Compton hump. Considering upper ranges between 12–45 keV, the best spin estimate was found between  $a_* \approx 0.6 - 0.69$  giving reduced chi-square values from  $\chi^2/\nu = 0.4 - 0.8$ , with higher values obtained at extended energy ranges. Most importantly, the model consistently estimated the 90 per cent upper limit for spin at  $a_* = 0.75$ . For the other global parameters, we treat the *RXTE* results as second-tier, but find results consistent with the *ASCA* values:  $q \approx 2.5$  and  $i > 72^\circ$  (90 per cent).

We are cautious in interpreting this spin estimate using *RXTE* spectral fits, owing to the coarse ( $\sim 20$  per cent) energy resolution. However, we expect that *RXTE* should provide robust upper bounds on the degree of relativistic broadening (viz., spin), owing to its vast collecting area and  $\lesssim 1$  per cent spectral calibration (Jahoda et al. 2006). We caution towards the significance of the *RXTE*-derived spin parameter and consider the upper limit obtained here as a *complementary result* to that obtained from the *ASCA* data alone, confirming that Fe-*K* $\alpha$  spin is not high.

## 7 DISCUSSION

### 7.1 A Combined Fe-*K* $\alpha$ and CF Result

In the two previous sections, we concluded that both the Fe-line and CF methods predict moderate values of spin, which are quite consistent:  $0.33 < a_* < 0.70$  (*ASCA* only) and  $-0.11 < a_* < 0.71$ , respectively (90 per cent confidence). The CF spin result predicts a slightly narrower Fe-line feature than that found by the Fe-line analysis. Alternatively, the Fe-line measurements consistently favor a high inclination, and therefore require a lesser distance ( $D \approx 4 \text{ kpc}$ ), in order for the CF results to match.

Having obtained two independent measurements of the spin, we now combine them by convolving the individual spin probability distributions to obtain the joint distribution shown in Figure 13. Our synthesized result is then  $0.29 < a_* < 0.62$ , with a most probable value of  $a_* = 0.49$ . Remarkably, based on a model of binary evolution and the GRB collapsar model, Brown et al. (2007) predicted that J1550 formed with  $a_* \approx 0.5$ . We confirm their prediction.

<sup>5</sup> Because we have selected a homogeneous set of spectra with almost identical luminosities, it is likely that the emissivity index – an indicator of coronal geometry – is the same for all ten spectra.

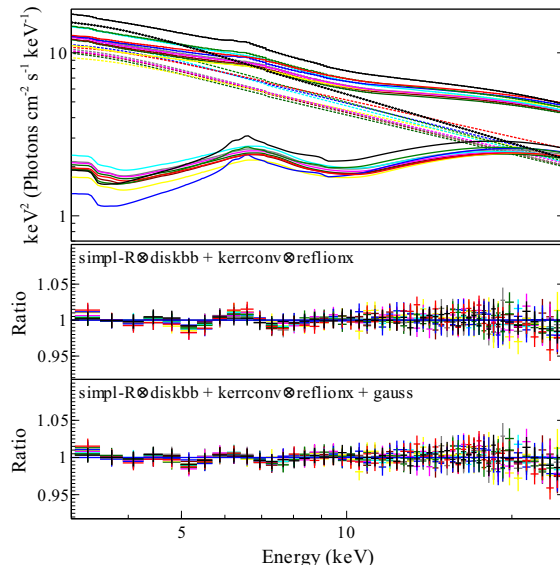


**Figure 12.** Best-fitting model (*top*) for the ten *RXTE* observations. The model consists of a disc and Compton continuum together with a relativistically blurred reflection component. The spin, inclination, and emissivity index were treated as global parameters (see § 6.3). (*middle:*) Data/model ratio for the above model and (*bottom:*) after the inclusion of a narrow Gaussian emission line.

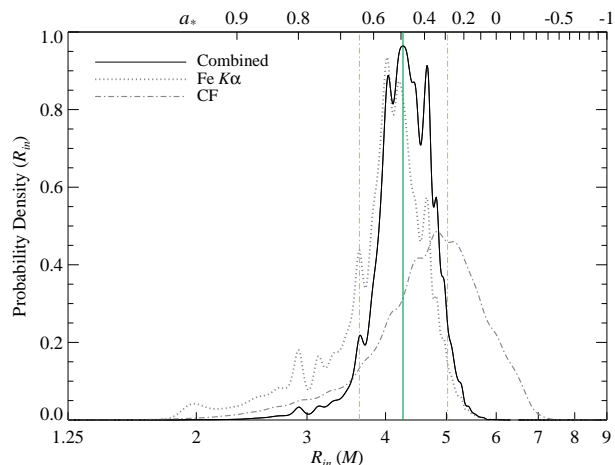


**Figure 13.** Combined Fe-*K* $\alpha$  and CF probability density for  $R_{\text{in}}$  and  $a_*$ . The net result is again a moderate value in-between the two individual estimates ( $a_* = 0.49^{+0.13}_{-0.20}$ , 90 per cent confidence).

### 7.2 Confronting GRMHD Simulations

Recently, it has become feasible, via general-relativistic magnetohydrodynamic (GRMHD) simulations, to assess the differences between MRI-driven accretion flows and the idealised  $\alpha$ -disc model, upon which our CF model is based. These differences include both a non-zero torque inside the ISCO and an altered angular momentum profile for the disc. The results of Penna et al. (2010) show, for the geometrically thin accretion discs we consider, that these effects are expected to impact our results by  $\lesssim 7$  per cent in  $r_{\text{in}}$  (roughly  $\Delta a_* \lesssim 0.09$  here). In general, they conclude that deviations from the Novikov-Thorne model are small for thin

discs at low luminosity and grow worse as the luminosity rises and the disc thickens.

Similar MHD simulations have been made to assess a principal assumption of the Fe-line method, namely, that the line emission from within the ISCO is negligible (Reynolds & Fabian 2008). Including the effect of contributing plunging-region emission results in intrinsically broader line profiles and hence will lower the estimate for spin. For the disc thickness and spin values in question, simulations predict that this effect could possibly shift  $r_{\text{in}}$  by  $\sim 12$  per cent (value taken from Fig. 5 in Reynolds & Fabian 2008), thereby decreasing the most probable Fe- $K\alpha$  estimate of spin from  $a_* \approx 0.55$  to  $\approx 0.4$ , in very close agreement with the best CF value of  $a_* \approx 0.34$ .

We infer that both spin estimates are subject to moderate corrections. For the Fe- $K\alpha$  reflection method, we can specifically conclude that the corrected value of spin is lower than the measured value, strengthening our conclusion that the spin of J1550 is moderate.

### 7.3 The Question of Alignment

The spin of an accreting black hole in a binary is expected to align with the orbital angular momentum vector of the system within  $\approx 10^7 - 10^8$  years (Maccarone 2002). A recent population synthesis study, which makes conservative assumptions concerning the torques acting to align a black hole, predicts that most black holes will be aligned to better than  $10^\circ$ . In § 6, we constrained the inclination of the inner, reflecting portion of the accretion disc (Fig. 10). This allows us to check on the relative alignment of the black hole spin axis (which is aligned with this inner-disc region; Lodato & Pringle 2006) and the orbital vector. In our exploration of the Fe- $K\alpha$  model, for a wide range of orbital inclinations ( $60^\circ - 82^\circ$ ), we find a best-fitting inclination for the inner disc of  $\approx 75 - 82^\circ$ . This value is consistent with the orbital inclination angle given by our dynamical model,  $i = 74.7 \pm 3.8$  (Orosz et al. 2010), which validates the CF assumption of alignment (Li et al. 2005), while simultaneously providing support for the dynamical model.

### 7.4 Implications of a Low-Spin Microquasar

The low spins of J1550 and the microquasar A0620–00 ( $a_* \approx 0.1$ ; Gou et al. 2010) challenge the long-standing and widely-held belief that there is a strong connection between black hole spin and relativistic jets (Blandford & Znajek 1977; hereafter BZ). We note that this belief is also challenged by a statistical study that found no evidence for a link between black hole spin and jet power (Fender et al. 2010). In any case, if jets are powered by black hole spin, then theory predicts that jet power will increase dramatically with increasing  $a_*$  (Tchekhovskoy et al. 2010), with the jet receiving more power from the accretion disc than from the black hole for  $a_* > 0.4$  (McKinney 2005).

Given the low spins of J1550 and A0620–00, it would appear that their episodic jets are driven largely by the accretion disc. One well-known candidate mechanism is the centrifugally driven outflow of matter from a disc described by Blandford & Payne 1982 (hereafter BP). A useful comparison of the operational regimes of BP and BZ is given by

Garofalo et al. (2010). They show that BP is always viable, but that BZ is a more likely mechanism for the most rapidly rotating sources, such as the extreme-Kerr BH microquasar GRS 1915+105 (McClintock et al. 2006; Blum et al. 2009).

The relativistic, two-sided jet of J1550 was launched during the remarkable 7 Crab flare (see § 1). We now show that during this daylong event the luminosity of the accretion disc was close to, or perhaps at, its Eddington limit, which suggests that radiation pressure was a key agent in collimating or feeding a magnetically-accelerated jet via a disc wind (for a discussion of the interplay between jet and wind, see Neilsen & Lee 2009 and Miller et al. 2008). In Figure 14, we plot the intrinsic accretion-disc luminosity during the flare state versus the luminosity during the thermal-dominant plateau state (Days 105–182; see Fig. 1). Each data point represents a single triplet of values of  $M$ ,  $i$  and  $D$  from among the 42,500 triplets considered in our Odyssey cluster analysis (Appendix A.4), and that data point was derived by analysing the complete data set for J1550. The spin for each point (averaged over the *gold* and *silver* data) is indicated by a colour, which is encoded in the bar at the top of the plot. The point corresponding to the dynamical model adopted by Orosz et al. (2010), Model F, which is our fiducial model, is labelled and marked by a red cross. The five less probable models considered by Orosz et al. are marked by black crosses. We conclude that Model F, by far the most probable model (see Appendix A.5), is very near the Eddington limit for disc accretion.

Luminous discs are geometrically thick and widely believed to be effective at driving jets. In the case of the J1550 flare, the disc is not only thick, it is also near its Eddington limit, so that it will provide substantial radiation pressure and possibly even shed material via a radiation-driven outflow, thereby promoting a jet-ejection event. In any case, as a bottom line, the low spins of J1550 and A0620–00 indicate that spin is not the sole driver behind all powerful episodic jets.

## 8 CONCLUSION

For the first time in a single work, we have determined high-quality estimates of the spin of an accreting black hole using the two independent, leading methods. In our CF analysis, we carefully explored the sensitivity of our results to a wide range of model-dependent systematic errors and observational errors. We conclude that J1550 is a slowly spinning black hole with  $a_* \approx 0.34$ , while ruling out spins larger than  $a_* \gtrsim 0.71$  at 90 per cent confidence. Next, we analysed the Fe- $K\alpha$  and reflection signatures in bright, intermediate spectral states of J1550. By modeling these broad, skewed features, we obtained a slightly higher estimate of the spin,  $a_* \approx 0.55^{+0.15}_{-0.22}$  (at 90 per cent confidence), while also deriving an estimate of the inclination angle of the inner disc that is in close agreement with the orbital inclination angle (Orosz et al. 2010). Combining the two spin estimates, we conclude that J1550, like the microquasar A0620–00, is a slowly spinning black hole.

The low spins of both J1550 and A0620–00 indicate that, for at least some microquasars, BZ-type mechanisms are not primary in driving powerful episodic jets, and that other mechanisms (perhaps BP) are at play. The near

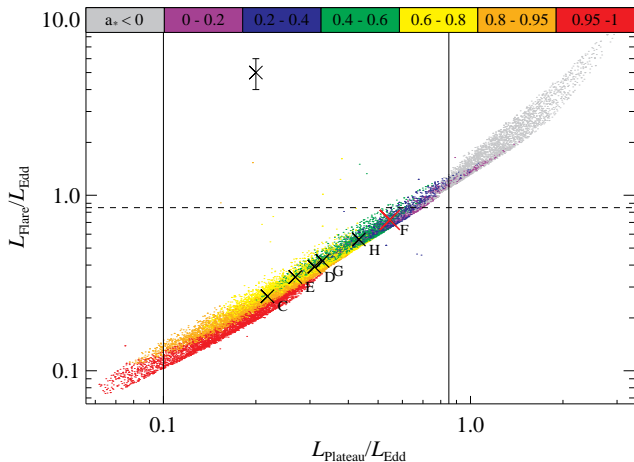


**Figure 14.** The intrinsic (i.e., seed) luminosity of the disc component during the 7 Crab flare versus the luminosity during the thermal plateau phase. In order to avoid saturating the plot, we show only half the data points, which were selected at random. The vertical black lines mark the lower and upper luminosity thresholds, and the horizontal dashed line corresponds to the Eddington limit of an accretion disc (§ 5). Note that Model F is very near this limit.

Eddington-limited 7 Crab flare observed for J1550 suggests that radiation-pressure support from a thermal disc is one possible way that low-spin black holes are aided in driving large-scale relativistic jets.

## ACKNOWLEDGMENTS

JFS was supported by the Smithsonian Institution Endowment Funds and JEM acknowledges support from NASA grant NNX08AJ55G. RN acknowledges support from NASA grant NNX08AH32G and NSF grant AST-0805832. RCR would like to thank the Science and Technology Research Council (STFC) and the Smithsonian Astrophysical Observatory for financial support. JFS thanks Bob Penna and Sasha Tchekhovskoy for helpful discussions, and the FAS Sciences Division Research Computing Group for their technical support with analyses performed on the Odyssey cluster.

## APPENDIX A: CONTINUUM-FITTING: ASSESSING THE SYSTEMATIC UNCERTAINTIES

### A1 Model Parameters

We consider the effect of the principal parameters listed in Table 3 on our final determination of the spin (Figure 6) for Model S (§ 3) and Model I (§ 4). Here and below, we consider only the *gold* data. As in §§ 3.2,4.2, we fix  $M$ ,  $i$ , and  $D$  at their fiducial values (§ 1). As illustrated in Figure 6, the effect of decreasing the viscosity parameter (P1 in Table 3) is to decrease  $r_{\text{in}}$  (by  $\sim 3 - 6$  per cent, depending on the model).

We allow the column density (P2-3) to vary over a broad range,  $N_{\text{H}} = 6 - 10 \times 10^{21} \text{ cm}^{-2}$ , which corresponds to  $\gtrsim 8\sigma$  relative to the precise value determined using *Chandra* grating data (see § 3.2). We consider this extreme range because of the discrepant results for  $N_{\text{H}}$  obtained using *ASCA* data (see § 6), which we attribute to an error in the calibration of the *ASCA* detectors at low energies. As shown in Table 3, our liberal estimate of the uncertainty in  $N_{\text{H}}$  affects our determination of  $r_{\text{in}}$  by  $< 3$  per cent.

We next explore the parameters of the IREFLECT model. We test smaller covering factors of 1/2 and 1/10 by linking the covering factor in IREFLECT to  $-(x-1)$  from the SIMPL-R model, where the leading minus sign acts as a switch in the model to isolate reflection from the direct (illuminating) component. Thus, we consider two cases:  $x = 1.5$  (P4) and  $x = 1.1$  (P5). We next try fitting for the covering factor, allowing it to vary between 0 and 1, while also fitting for the emissivity, which we constrain to lie in the range  $2 < q < 5$  (P6). As shown in Table 3, the effect of this exercise on  $r_{\text{in}}$  is small  $\approx 1$  per cent. Smaller still is the effect of varying the disc temperature. Decreasing  $T_{\text{disc}}$  (P7) by a factor of 5 relative to its assumed value (§ 4.2), we find that the ionisation parameter increases slightly, but that the effect on  $r_{\text{in}}$  is negligible ( $< 0.1$  per cent).

Lastly, we adjust the width of the SMEDGE component  $W_{\text{Edge}}$  to first half (P8) and then twice (P9) its nominal value of 7 keV, which impacts  $r_{\text{in}}$  by  $< 0.5$  per cent.

In summary, as we found earlier in our study of LMC X-3 (Steiner et al. 2010),  $\alpha$  is the parameter (aside from  $M$ ,  $i$ , and  $D$ ) that introduces the largest uncertainty in determining spin via the CF method.

### A2 Model Components

We begin by substituting BHSPEC (Davis & Hubeny 2006) for the thermal disc component in place of KERRBB2 (see § 4.2 in McClintock et al. 2006 for a discussion of these relativistic disc models and their relationship). The virtue of BHSPEC relative to KERRBB2 is that it directly computes the effects of spectral hardening; its drawback is that it does not include returning radiation, which heats the disc. Employing BHSPEC and following the procedures described in the preceding section, we find that  $r_{\text{in}}$  is increased by  $\approx 1 - 3$  per cent (M1 in Table 3).

Next, we explore the possibility that the power-law component is cut off exponentially at high energy (e.g., thermal Comptonisation), while allowing the cut-off energy to vary over the range  $kT_e = 25 - 200$  keV. (We did not correct  $f_{\text{sc}}$  in order to achieve photon conservation because this correction is negligible for the *gold* spectra.) We find that the effect of a possible cutoff is small, changing  $r_{\text{in}}$  by  $\lesssim 1.5$  per cent (M2). In addition, we generated the power law using the double-sided version of SIMPL and SIMPL-R (in place of the upscattering-only version). The effect on  $r_{\text{in}}$  is  $\lesssim 0.3$  per cent (M3).

Lastly, we examine the effects of substituting one of the reflection components for another. We find that both IREFLECT and REFLIONX give somewhat smaller values of  $r_{\text{in}}$  than SMEDGE, but the effect is small,  $\lesssim 3$  per cent (M4, M5).



### A3 Flux

As described in § 5, we include a liberal  $\sim 10$  per cent allowance for the uncertainty in the absolute-flux calibration. Because the luminosity of the thermal component at a given colour temperature scales proportionally to  $r_{\text{in}}^2$ , a 10 per cent adjustment to the flux normalisation introduces a 5 per cent uncertainty in  $r_{\text{in}}$ .

### A4 Black Hole Mass, Inclination and Distance

While analysing the X-ray spectral data, we have used the best estimates for  $M$ ,  $i$  and  $D$  (§ 1) taken from Model F of Table 1 in Orosz et al. (2010). To explore the sensitivity of spin to uncertainties in these measured values, we use the Odyssey computing cluster at Harvard University and fit the data set at each point in a 3-D grid of 42,500 points distributed uniformly over mass, inclination, and distance. The grid spans the ranges  $M = 5 - 17.5 M_{\odot}$ ,  $i = 36 - 85^{\circ}$  and  $D = 3 - 7$  kpc, respectively. We adopt the 3 kpc distance bound following Hannikainen et al. (2009); the 7 kpc bound is a relativistic limit based on the proper motion of the X-ray jets (Corbel et al. 2002):  $D \leq c/\sqrt{\mu_{\alpha}\mu_{\delta}} \lesssim 7$  kpc (e.g., Mirabel & Rodríguez 1999). At each grid point, we compute a table of the spectral hardening factor (e.g., see Gou et al. 2010) and fit all of the available TD, SPL, and INT spectra. We use Model S (§ 3.2) because it is computationally efficient and has the best performance of all three CF models considered. We perform the analysis for both values of disc viscosity:  $\alpha = 0.01$  and  $\alpha = 0.1$ .

We then apply our data selection criteria, obtaining a sample of *gold* and *silver* spectra (typically 50–100) at each of the 42,500 grid points. From this we derive a spin probability distribution unique to each point. Before summing over the grid, we impose the following grid point selection constraints: First, the grid point’s inclination must be below the eclipsing limit,  $i < 82^{\circ}$  (see e.g., Narayan & McClintock 2005). Secondly, as discussed in § 5, we require that the intrinsic disc luminosity during the TD-state plateau phase (days 105–181; Figure 1) fall in the range  $0.10 < L_{\text{D}}/L_{\text{Edd}} < 0.85$ . We combine the distributions for all satisfactory grid points, weighting each according to its location in the grid (with high weights occurring at probable values of  $M$ ,  $i$ , and  $D$ ).

### A5 Rolling Together the Uncertainties

We combine the systematic uncertainties discussed above in two stages. Referring to Table 3, in the first stage we combine in quadrature the individual values in the Model S column for rows P8-9, M1, M2-3, M4-5 with half the value for P2-3 (half because the range of variation considered for  $N_{\text{H}}$  is so extreme). For each of the parameters  $N_{\text{H}}$  and  $W_{\text{Edge}}$ , we use the larger of the deviations given in the table. The resultant error of 4.2 per cent is combined with the 5 per cent error in  $r_{\text{in}}$  from flux uncertainty to give a net error of 6.5 per cent. This combined uncertainty sets the half-length for a boxcar smoothing kernel that we apply to the full spin distribution.

The resulting distribution is shown in Figure A1. Because we have so far considered just dynamical Model F, the distribution of  $r_{\text{in}}$  is narrower,  $-0.14 < a_* < 0.57$  (90 per cent confidence level) than our final distribution shown

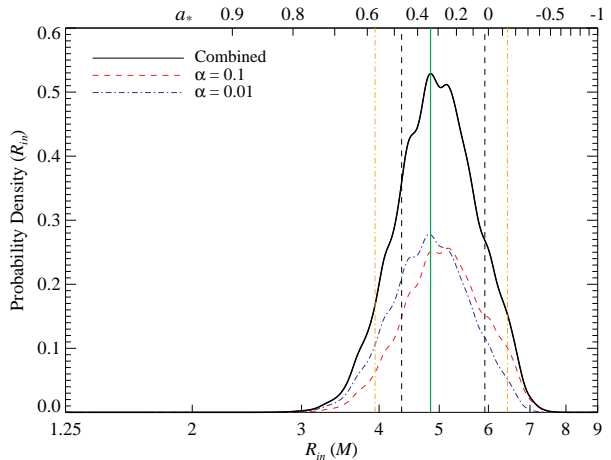


**Figure A1.** Similar to Figure 6, but using just Model F in Orosz et al. (2010). The green, black, and gold vertical lines indicate the most likely value for  $R_{\text{in}}$  ( $a_*$ ), and  $1\sigma$  and 90 per cent confidence interval limits, respectively.

in Figure 6, although the most probable value of spin is unchanged,  $a_* = 0.34$ . We now go on to the second stage in combining sources of error and consider an ensemble of possible dynamical models.

The case of J1550 is unusual in that there are several candidate models which produce reasonable fits to the dynamical data, which are summarized in Table 1 in Orosz et al. (2010). Above, we considered only Model F, the most probable model. We now incorporate the possibility that one of the five alternative models (Models C-E and Models G & H) are correct. Models A and B do not constrain the dynamical model satisfactorily, and do not allow one to obtain a useful distance estimate, and so they are disregarded here.

As was done above for Model F, a spin ( $r_{\text{in}}$ ) probability distribution is obtained for each candidate dynamical model. We use for each model, including Model F, the total  $\chi^2$  (summed for the velocity data and the light curve data, both optical and infrared) to determine its corrected Akaike Information Criterion (AICc; Akaike 1974; Hurvich & Tsai 1989), which is closely related to the log-likelihood of each model. Using these values, AIC-weights are assigned to each model ( $i$ ):  $W_{\text{AIC}, i} = \text{Exp}[-1/2 (\text{AICc}_i - \text{inf}\{\text{AICc}\})]$  (Burnham & Anderson 2002).

Our fiducial dynamical model is by far the most likely, carrying  $\sim 84$  per cent of the total weight. A weighted sum is computed using the AIC-weights to obtain a composite spin distribution. This is broadened using the boxcar smoothing kernel described above (13 per cent width) to produce the final distribution as shown in Figure 6. *Thus, this final result incorporates uncertainties in the choice of the dynamical model; dynamical model uncertainties; the X-ray spectral model and model parameter settings as summarized in Table 3; and a 10 per cent uncertainty in the X-ray flux calibration.*

## REFERENCES

- Akaike H., 1974, *Automatic Control*, IEEE Transactions on, 19, 716
- Arnaud K. A., 1996, in Jacoby G. H., Barnes J., eds, *Astronomical Data Analysis Software and Systems V* Vol. 101 of *Astronomical Society of the Pacific Conference Series*, XSPEC: The First Ten Years. p. 17
- Arvanitaki A., Dimopoulos S., Dubovsky S., Kaloper N., March-Russell J., 2010, *Phys. Rev. D*, 81, 123530
- Beloborodov A. M., 1999, *ApJ*, 510, L123
- Berti E., Volonteri M., 2008, *ApJ*, 684, 822
- Blandford R. D., Payne D. G., 1982, *MNRAS*, 199, 883
- Blandford R. D., Znajek R. L., 1977, *MNRAS*, 179, 433
- Blum J. L., Miller J. M., Fabian A. C., Miller M. C., Homan J., van der Klis M., Cackett E. M., Reis R. C., 2009, *ApJ*, 706, 60
- Brenneman L. W., Reynolds C. S., 2006, *ApJ*, 652, 1028
- Brown G. E., Lee C., Moreno Méndez E., 2007, *ApJ*, 671, L41
- Burnham K. P., Anderson D. R., 2002, *Model Selection and Multimodel Inference*. New York, Springer-Verlag New York, Inc.
- Campanelli M., Lousto C. O., Zlochower Y., 2006, *Phys. Rev. D*, 74, 041501
- Corbel S., Fender R. P., Tzioumis A. K., Tomsick J. A., Orosz J. A., Miller J. M., Wijnands R., Kaaret P., 2002, *Science*, 298, 196
- Corbel S., Kaaret P., Jain R. K., Bailyn C. D., Fender R. P., Tomsick J. A., Kalemci E., McIntyre V., Campbell-Wilson D., Miller J. M., McCollough M. L., 2001, *ApJ*, 554, 43
- Davis S. W., Blaes O. M., Hubeny I., Turner N. J., 2005, *ApJ*, 621, 372
- Davis S. W., Done C., Blaes O. M., 2006, *ApJ*, 647, 525
- Davis S. W., Hubeny I., 2006, *ApJS*, 164, 530
- Done C., Mulchaey J. S., Mushotzky R. F., Arnaud K. A., 1992, *ApJ*, 395, 275
- Dunn R. J. H., Fender R. P., Körding E. G., Belloni T., Cabanac C., 2010, *MNRAS*, 403, 61
- Ebisawa K., 1999, in Poutanen J., Svensson R., eds, *High Energy Processes in Accreting Black Holes* Vol. 161 of *ASP Conference Series*, X-ray Energy Spectra of Galactic Black Hole Candidates. pp 39–53
- Ebisawa K., Ogawa M., Aoki T., Dotani T., Takizawa M., Tanaka Y., Yoshida K., Miyamoto S., Iga S., Hayashida K., Kitamoto S., Terada K., 1994, *PASJ*, 46, 375
- Esin A. A., McClintock J. E., Narayan R., 1997, *ApJ*, 489, 865
- Fabian A. C., Rees M. J., Stella L., White N. E., 1989, *MNRAS*, 238, 729
- Fabian A. C., Zoghbi A., Ross R. R., Uttley P., Gallo L. C., Brandt W. N., Blustin A. J., Boller T., Caballero-Garcia M. D., Larsson J., Miller J. M., Miniutti G., Ponti G., Reis R. C., Reynolds C. S., Tanaka Y., Young A. J., 2009, *Nat*, 459, 540
- Fender R. P., Gallo E., Russell D., 2010, *MNRAS*, pp 1009–+
- García J., Kallman T. R., 2010, *ApJ*, 718, 695
- Garofalo D., Evans D. A., Sambruna R. M., 2010, *MNRAS*, 406, 975
- Gierliński M., Done C., 2003, *MNRAS*, 342, 1083
- Gou L., McClintock J. E., Steiner J. F., Narayan R., Cantrell A. G., Bailyn C. D., Orosz J. A., 2010, *ApJ*, 718, L122
- Gou L. J., McClintock J. E., Liu J., Narayan R., Steiner J. F., Remillard R. A., Orosz J. A., Davis S. W., Ebisawa K., Schlegel E. M., 2009, *ApJ*, 701, 1076
- Hannikainen D. C., Hunstead R. W., Wu K., McIntyre V., Lovell J. E. J., Campbell-Wilson D., McCollough M. L., Reynolds J., Tzioumis A. K., 2009, *MNRAS*, 397, 569
- Homan J., Wijnands R., van der Klis M., Belloni T., van Paradijs J., Klein-Wolt M., Fender R., Méndez M., 2001, *ApJS*, 132, 377
- Hurvich C. M., Tsai C.-L., 1989, *Biometrika*, 76, 297
- Jahoda K., Markwardt C. B., Radeva Y., Rots A. H., Stark M. J., Swank J. H., Strohmayer T. E., Zhang W., 2006, *ApJS*, 163, 401
- Johannsen T., Psaltis D., 2010, *ApJ*, 716, 187
- King A. R., Pringle J. E., Livio M., 2007, *MNRAS*, 376, 1740
- Kubota A., Done C., 2004, *MNRAS*, 353, 980
- Laor A., 1991, *ApJ*, 376, 90
- Lee C., Brown G. E., Wijers R. A. M. J., 2002, *ApJ*, 575, 996
- Li L.-X., Zimmerman E. R., Narayan R., McClintock J. E., 2005, *ApJS*, 157, 335
- Liu J., McClintock J. E., Narayan R., Davis S. W., Orosz J. A., 2008, *ApJ*, 679, L37
- Liu J., McClintock J. E., Narayan R., Davis S. W., Orosz J. A., 2010, *ApJ*, 719, L109+
- Lodato G., Pringle J. E., 2006, *MNRAS*, 368, 1196
- Maccarone T. J., 2002, *MNRAS*, 336, 1371
- Magdziarz P., Zdziarski A. A., 1995, *MNRAS*, 273, 837
- McClintock J. E., Remillard R. A., Rupen M. P., Torres M. A. P., Steeghs D., Levine A. M., Orosz J. A., 2009, *ApJ*, 698, 1398
- McClintock J. E., Shafee R., Narayan R., Remillard R. A., Davis S. W., Li L.-X., 2006, *ApJ*, 652, 518
- McKinney J. C., 2005, *ApJ*, 630, L5
- McNamara B. R., Kazemzadeh F., Rafferty D. A., Birzan L., Nulsen P. E. J., Kirkpatrick C. C., Wise M. W., 2009, *ApJ*, 698, 594
- Miller J. M., 2007, *ARA&A*, 45, 441
- Miller J. M., Cackett E. M., Reis R. C., 2009, *ApJ*, 707, L77
- Miller J. M., Fabian A. C., Nowak M. A., Lewin W. H. G., 2005, in M. Novello, S. Perez Bergliaffa, & R. Ruffini ed., *The Tenth Marcel Grossmann Meeting. On recent developments in theoretical and experimental general relativity, gravitation and relativistic field theories* Relativistic Iron Lines in Galactic Black Holes: Recent Results and Lines in the ASCA Archive. pp 1296–+
- Miller J. M., Marshall H. L., Wijnands R., Di Matteo T., Fox D. W., Kommers J., Pooley D., Belloni T., Casares J., Charles P. A., Fabian A. C., van der Klis M., Lewin W. H. G., 2003, *MNRAS*, 338, 7
- Miller J. M., Raymond J., Reynolds C. S., Fabian A. C., Kallman T. R., Homan J., 2008, *ApJ*, 680, 1359
- Miller J. M., Reynolds C. S., Fabian A. C., Miniutti G., Gallo L. C., 2009, *ApJ*, 697, 900
- Miniutti G., Panessa F., de Rosa A., Fabian A. C., Malizia A., Molina M., Miller J. M., Vaughan S., 2009, *MNRAS*, 398, 255

- Mirabel I. F., Rodríguez L. F., 1999, *ARA&A*, 37, 409
- Mitsuda K., Inoue H., Koyama K., Makishima K., Matsumoto M., Ogawara Y., Suzuki K., Tanaka Y., Shibazaki N., Hirano T., 1984, *PASJ*, 36, 741
- Narayan R., McClintock J. E., 2005, *ApJ*, 623, 1017
- Neilsen J., Lee J. C., 2009, *Nat*, 458, 481
- Noble S. C., Krolik J. H., Hawley J. F., 2009, *ApJ*, 692, 411
- Noble S. C., Krolik J. H., Hawley J. F., 2010, *ApJ*, 711, 959
- Novikov I. D., Thorne K. S., 1973, in *Black Holes (Les Astres Occlus) Astrophysics of black holes..* pp 343–450
- Orosz J. A., Groot P. J., van der Klis M., McClintock J. E., Garcia M. R., Zhao P., Jain R. K., Bailyn C. D., Remillard R. A., 2002, *ApJ*, 568, 845
- Orosz J. A., Steiner J. F., McClintock J. E., 2010, *TEMP ApJ*
- Penna R. F., McKinney J. C., Narayan R., Tchekhovskoy A., Shafee R., McClintock J. E., 2010, arXiv:1003.0966
- Reis R. C., Fabian A. C., Ross R. R., Miller J. M., 2009, *MNRAS*, 395, 1257
- Reis R. C., Fabian A. C., Ross R. R., Miniutti G., Miller J. M., Reynolds C., 2008, *MNRAS*, 387, 1489
- Reis R. C., Miller J. M., Fabian A. C., Cackett E. M., Maitra D., Reynolds C. S., Rupen M., Steeghs D. T. H., Wijnands R., 2010, ArXiv e-prints
- Remillard R. A., McClintock J. E., 2006, *ARA&A*, 44, 49
- Remillard R. A., Sobczak G. J., Munro M. P., McClintock J. E., 2002, *ApJ*, 564, 962
- Reynolds C. S., Fabian A. C., 2008, *ApJ*, 675, 1048
- Reynolds C. S., Nowak M. A., 2003, *Phys. Rep.*, 377, 389
- Ross R. R., Fabian A. C., 1993, *MNRAS*, 261, 74
- Ross R. R., Fabian A. C., 2005, *MNRAS*, 358, 211
- Ross R. R., Fabian A. C., 2007, *MNRAS*, 381, 1697
- Ross R. R., Fabian A. C., Brandt W. N., 1996, *MNRAS*, 278, 1082
- Schmoll S., Miller J. M., Volonteri M., Cackett E., Reynolds C. S., Fabian A. C., Brenneman L. W., Miniutti G., Gallo L. C., 2009, *ApJ*, 703, 2171
- Shafee R., McClintock J. E., Narayan R., Davis S. W., Li L.-X., Remillard R. A., 2006, *ApJ*, 636, L113
- Shafee R., McKinney J. C., Narayan R., Tchekhovskoy A., Gammie C. F., McClintock J. E., 2008, *ApJ*, 687, L25
- Shapiro S. L., Teukolsky S. A., 1983, *Black holes, white dwarfs, and neutron stars: The physics of compact objects.* New York, Wiley-Interscience
- Sobczak G. J., McClintock J. E., Remillard R. A., Cui W., Levine A. M., Morgan E. H., Orosz J. A., Bailyn C. D., 2000, *ApJ*, 544, 993
- Steiner J. F., McClintock J. E., Remillard R. A., Gou L., Yamada S., Narayan R., 2010, *ApJ*, 718, L117
- Steiner J. F., McClintock J. E., Remillard R. A., Narayan R., Gou L. J., 2009, *ApJ*, 701, L83
- Steiner J. F., Narayan R., McClintock J. E., Ebisawa K., 2009, *PASP*, 121, 1279
- Tanaka Y., Lewin W. H. G., 1995, in W. H. G. Lewin, J. van Paradijs, & E. P. J. van den Heuvel ed., *X-ray binaries*, p. 126 - 174 *Black hole binaries..* pp 126–174
- Tchekhovskoy A., Narayan R., McKinney J. C., 2010, *ApJ*, 711, 50
- Tomsick J. A., Corbel S., Kaaret P., 2001, *ApJ*, 563, 229
- Toor A., Seward F. D., 1974, *AJ*, 79, 995
- Valinia A., Marshall F. E., 1998, *ApJ*, 505, 134
- Volonteri M., Madau P., Quataert E., Rees M. J., 2005, *ApJ*, 620, 69
- Weisskopf M. C., Guainazzi M., Jahoda K., Shaposhnikov N., O’Dell S. L., Zavlin V. E., Wilson-Hodge C., Elsner R. F., 2010, *ApJ*, 713, 912
- Wilms J., Allen A., McCray R., 2000, *ApJ*, 542, 914
- Woosley S. E., 1993, *ApJ*, 405, 273
- Xue Y., Wu X., Cui W., 2008, *MNRAS*, 384, 440
- Zhang S. N., Cui W., Chen W., 1997, *ApJ*, 482, L155+
- Zoghbi A., Fabian A. C., Uttley P., Miniutti G., Gallo L. C., Reynolds C. S., Miller J. M., Ponti G., 2010, *MNRAS*, 401, 2419